LITHOS 470-471 (2024) 107504

Contents lists available at ScienceDirect

LITHOS

journal homepage: www.elsevier.com/locate/lithos

Ages, geochemistry and Sr-Nd-Pb isotopes of alkaline potassic volcanic rocks from the Ahar-Arasbaran region (NW Iran): Evidence for progressive evolution of mantle sources during the Neotethyan subduction system

C. Natali [a,g,*,1], M. Aghazadeh [b,1,*], E. Braschi [c,a], R. Avanzinelli [a,c], Z. Badrzadeh [b], G. Bianchini [d], M. Casalini [a,g], S. Agostini [e], M. Mattei [f], S. Conticelli [a,f,g,*]

[a] Dipartimento di Scienze della Terra, Università degli studi di Firenze, Via Giorgio La Pira, 4, Firenze I-50121, Italy
[b] Department of Geology, Payame Noor University, Tehran, Iran
[c] CNR - Istituto di Geoscienze e Georisorse, Unità di Firenze, Via Giorgio La Pira, 4, Firenze I-50121, Italy
[d] Dipartimento di Fisica e Scienze della Terra, Università degli studi di Ferrara, Via Giuseppe Saragat, 1, Ferrara 44124, Italy
[e] CNR - Istituto di Geoscienze e Georisorse, Unità di Pisa, Area Territoriale di Ricerca di Pisa, Via G. Moruzzi, 1, Pisa I-56124, Italy
[f] Dipartimento di Scienze, Università degli studi di Roma III, Largo San Leonardo Murialdo, 1, Roma I-00146, Italy
[g] CNR - Istituto di Geologia Ambientale e Geoingegneria, Unità di Montelibretti, Area Territoriale di Ricerca di Roma 1, Strada Provinciale 35d, 9, Montelibretti (RM) I-00010, Italy

ARTICLE INFO

Keywords:
Arasbaran volcanism
Neotethys subduction
Ultrapotassic volcanic rocks
Geochronology
Geochemistry
Sr-Nd-Pb isotopes

ABSTRACT

The volcanism of the Arasbaran region, northwest Iran, is characterized by multiple magmatic pulses from Cretaceous to Quaternary related to the consumption of the Neotethys oceanic basin and the subsequent continental collision between the Arabia and the Eurasian plates. In this paper we focus on the Eocene igneous products, which show wide compositional variations, ranging from shoshonite to tephrite and phonolite. They may be further grouped into leucite (analcime)-bearing and leucite-free rock types on the basis of their rock-forming minerals. Leucite-bearing and leucite-free Eocene magmatic rocks are geographically separate outcropping in the WNW and ESE part of the Ahar-Arasbaran region, respectively. K—Ar dating show leucite-bearing rocks (39.4–39.6 +/− 1.0 Ma) being slightly younger with respect to leucite-free rocks (41.0–41.9 +/− 1.0 Ma). The two rock types are differentiated by each other in terms of silica saturation degrees but display similar incompatible trace elements distributions, typical of subduction-related volcanic rocks. Indeed, clear depletions in HFSE (e.g., Nb, Ta, Ti, Zr) and enrichments in LILE (e.g., Ba, K) and Pb are shown. The leucite-bearing volcanic rocks are strongly silica-undersaturated (Δq ca. -35) and show higher LILE/HFSE, LILE/REE, Ba/La (30–90) and Ba/Th (up to 520) values with respect to leucite-free rocks (Δq from 0 to −15; Ba/La up to 30). Leucite-bearing and -free groups also show distinct Sr-Nd-Pb isotopic compositions, with the former having less radiogenic Sr ($^{87}Sr/^{86}Sr$ 0.704424–0.704634) and Pb ($^{206}Pb/^{204}Pb$ 18.58–18.65, $^{207}Pb/^{204}Pb$ 15.57–15.60, $^{208}Pb/^{204}Pb$ 38.63–38.71) and more radiogenic Nd ($^{143}Nd/^{144}Nd$ 0.512695–0.512791), with respect to the latter ones ($^{87}Sr/^{86}Sr$ 0.704481–0.705669, $^{206}Pb/^{204}Pb$ 18.65–18.75, $^{207}Pb/^{204}Pb$ 15.61–15.64, $^{208}Pb/^{204}Pb$ 38.65–38.87, $^{143}Nd/^{144}Nd$ 0.512572–0.512623). Geochemical and isotopic compositions, coupled with the strong silica-undersaturated character, of leucite-bearingrocks suggest in their mantle source the involvement of metasomatizing partial melts from subducted altered oceanic crust and subordinate carbonate-bearing sediments. On the other hand, the compositions of leucite-free igneous rocks are compatible with the involvement of a relatively higher contribution of partial melts from terrigenous (carbonate-poor) subducted sediments. The close spatial association and the relative geographical/stratigraphic position of these products indicate diachronous metasomatic events in the mantle wedge underlying the Arasbaran area that could have been originated by the late arrival of carbonate-rich sediments at depth during slab steepening and incipient roll-back preceding the continental collision. K —Ar dating indicates that the Arasbaran magmatism was triggered by a late geodynamic event, during middle Eocene, plausibly consisting of re-adjusting of isotherms that heated the veined mantle wedge following the slab migration after roll-back. The slightly younger age of leucite-bearing

* Corresponding authors.
E-mail addresses: claudio.natali@unifi.it (C. Natali), mehrajaghazadeh@pnu.ac.ir (M. Aghazadeh), sandro.conticelli@cnr.it (S. Conticelli).
[1] These authors contributed equally to this research

https://doi.org/10.1016/j.lithos.2024.107504
Received 6 October 2023; Received in revised form 11 January 2024; Accepted 13 January 2024
Available online 24 January 2024

rocks with respect to leucite-free rocks, coupled with the lower melting degree of the former may suggest an evolution of the local thermal regime with the progressive involvement of portions of the mantle wedge closer to the subducted plate.

1. Introduction

K-rich igneous rocks (shoshonitic and ultrapotassic) are common magmatic products at destructive plate margins and they span from oceanic-supra subduction active continental margin stage to syn and post-collisional stages (e.g., Avanzinelli et al., 2009; Conticelli et al., 2015; Lustrino and Wilson, 2007; Prelević et al., 2008). The origin of these magmas was attributed to the partial melting of a mantle source variably metasomatised by the addition of fluids/melts during the subduction of oceanic lithosphere under the continental margin (e.g., Avanzinelli et al., 2009; Conticelli et al., 2011, 2015; Elliott, 2003; Foley, 1992; Hart, 1984). The coexistence of K-rich magmas with various alkalinity degree was interpreted as a consequence of the involvement of a sedimentary component to the mantle source, coupled with a steepening and roll-back of the subducted plate in the late stage of convergence or in post-collisional settings (e.g., Conticelli et al., 2009, 2015; Conticelli and Peccerillo, 1992). The evolution of the Mesozoic Tethyan realm and development of the western sector of the Alpine-Himalayan belt, ultrapotassic and shoshonitic rocks were interpreted as the product of increasing partial melting degree of a metasomatised mantle source progressively involving the residual highest temperature liquidus domains (e.g., Avanzinelli et al., 2020; Dallai et al., 2019, 2022; Foley, 1992; Tommasini et al., 2011). In the Cenozoic magmatic evolution of western Mediterranean, many authors constrained this general hypothesis by petrographic, geochemical and isotopic data, providing comprehensive explanation for the genesis and the evolution of the magmatism in this very complex natural laboratory. Particular attention was devoted to potassic-rich rocks (shoshonitic and ultrapotassic) and the genesis of leucite-bearing and leucite-free magmas (e.g., Conticelli et al., 2011, 2015; Conticelli and Peccerillo, 1992; Prelević et al., 2005, 2008). The genesis of K-rich magmas was generally ascribed to various contribution of continental terrigenous and carbonate-bearing sediment/lithologies to the metasomatic agents in their mantle sources (Avanzinelli et al., 2009). Experimental studies indicate that mantle peridotite including hydrous, incompatible element-rich net veins derived from subducted sediments is a viable source for the generation of K-rich alkaline magmas (e.g., Avanzinelli et al., 2020; Bianchini et al., 2015; Foley, 1992). Thomsen and Schmidt (2008) demonstrated the capability to generate potassic granite or phonolite melts from carbonated pelites in the T-P range 950–1070 °C 2.4–5.0 GPa, suggesting that the involvement of a carbonate component in the mantle source could be responsible for the generation of silica-undersaturated magmas. In particular, strongly silica-undersaturated ultrapotassic leucite-bearing magmas are thought to be derived from a metasomatised upper mantle by partial melting of a phlogopite-bearing lherzolite or wehrlite characterized by a CO_2 excess with respect to H_2O, then high XCO_2 (e.g., Lloyd et al., 1985 and references therein), recalling the presence of a carbonate-bearing component in the metasomatized mantle sources (Avanzinelli et al., 2009, 2018; Boari et al., 2009; Bragagni et al., 2022; Conticelli et al., 2015; Conticelli and Peccerillo, 1992; Ren et al., 2023). On the other hand, the generation of high silica leucite-free ultrapotassic magmas is compatible with the partial melting of a phlogopite-bearing harzburgite produced by metasomatism by sediment melts under high XH_2O (Avanzinelli et al., 2009; Casalini et al., 2022; Conticelli et al., 2011; Prelević et al., 2008). Neogene to Quaternary ultrapotassic rocks of kamafugitic (SiO_2-poor) and lamproitic (SiO_2-rich) affinities also occur in the central-eastern Mediterranean sector of the Alpine-Himalayan belt, from the Balkans (Prelević et al., 2005) to western Anatolia (e.g., Akal, 2008; Casalini et al., 2022; Çoban and Flower, 2007; Dilek et al., 2010; Doglioni et al., 2002; Francalanci et al., 2000; Innocenti et al., 2005; Prelević et al., 2008, 2012, 2015) and were generally interpreted as the counterpart of western Mediterranean ultrapotassic rocks.

In the middle sector of the Alpine-Himalayan belt, extending from the Pontide Arc in Central-Eastern Anatolia to the Alborz mountain range in Iran, widespread Late Cretaceous to Quaternary subduction-related magmatism, including K-rich rocks, occurred in response to the diachronous (mainly Cenozoic) closure of Tethyan oceanic branches and subsequent continental collision of the Arabia-Eurasian plates (e.g., Dilek et al., 2010). In this sector, several occurrences of leucite-bearing and leucite-free ultrapotassic (often associated to shoshonitic) volcanic rocks are reported in the literature. This rock association is commonly recognized from Central (Gülmez et al., 2016) and Eastern Pontides, where plagioleucitites (Altherr et al., 2008) and shoshonitic leucite-free and ultrapotassic leucite-bearing rocks of Maastrichtian-early Paleocene age (Eyuboglu et al., 2011) outcrop, as well as in NW Iran. In particular, the Iranian area displays a heterogenous and complex rock assemblage and spatial distribution, with shoshonitic, leucite-free and ultrapotassic leucite-bearing rocks of Late Miocene age outcropping in the Eslamy Peninsula, (Lustrino et al., 2019 and references therein); high-K leucite-bearing and leucite-free rocks of Eocene age (Shafaii Moghadam et al., 2018; Soltanmohammadi et al., 2018, 2021) exposed in Lahrud area and Salavat range in the Ardabil province; leucite-bearing rocks of Eocene age in Moghan area (Amraee et al., 2019), Alborz Mountains (Aghazadeh et al., 2011) and Lesser Caucasus (Dilek et al., 2010; Lustrino et al., 2019). The numerous, different interpretations regarding the genesis of the different K-rich igneous rocks characterizing this complex area, mainly arise from the lack of systematic differences in their geochemical and isotopic features, with respect to their analogues in western Mediterranean. In fact, the relatively limited variability, especially in the isotopic composition, exhibited by leucite-free and leucite-bearing rocks from this sector poses several problems in the precise identification of the nature of the metasomatic agents affecting their mantle sources.

In this paper, we report new petrographic, geochemical, and isotopic composition, as well as new K—Ar age determination, of K-rich leucite-bearing and -free igneous rocks from the Ahar-Arasbaran region (NW Iran). This region is a key area in between the other localities we listed above, thus assessing the genesis of the coexisting leucite-bearing and leucite-free magmas can help improving the knowledge of the subduction-related Cenozoic volcanism of this sector of the Alpine-Himalayan belt, and better define the processes that characterized the diachronous closure of the Tethyan Realm.

2. Geological outline

The Ahar–Arasbaran region is located in the hinterland of the Arabia–Eurasia collision zone, in the broad Alpine–Himalayan orogenic belt (Fig. 1a). The area is part of the Turkish-Iranian Plateau (TIP), consisting of several pre-Mesozoic micro-continents accreted to the Eurasia margin as the result of the opening and closing of different branches of the Tethyan ocean (Soltanmohammadi et al., 2018). While the subduction of the Paleo-Tethys was active, from 360 to 210 Ma, along the Greater Caucasus and northern Iran (Stampfli, 2000), the successive subduction system of the Neotethys migrated southward from the Pontides arc and southwest Zagros, due the multiple arc-microcontinent collisions that prolonged up to the Cenozoic (Dilek et al., 2010 and references therein). Sengor and Yilmaz (1981) suggested a northward subduction of the Neotethyan ocean from the Upper Cretaceous until the end of the Eocene, which ended with the continental collision between Arabian and Eurasian plates (McQuarrie and van Hinsbergen, 2013). The partial

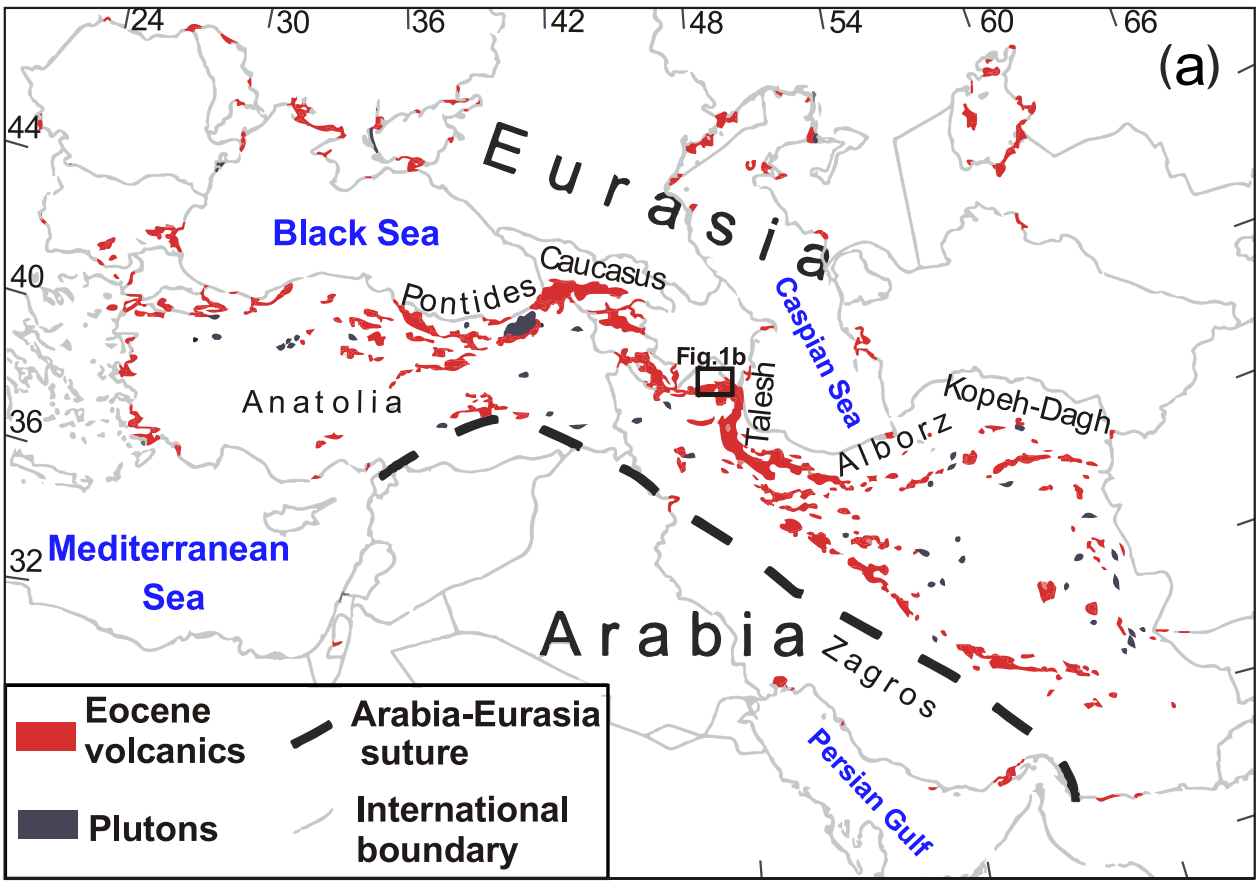

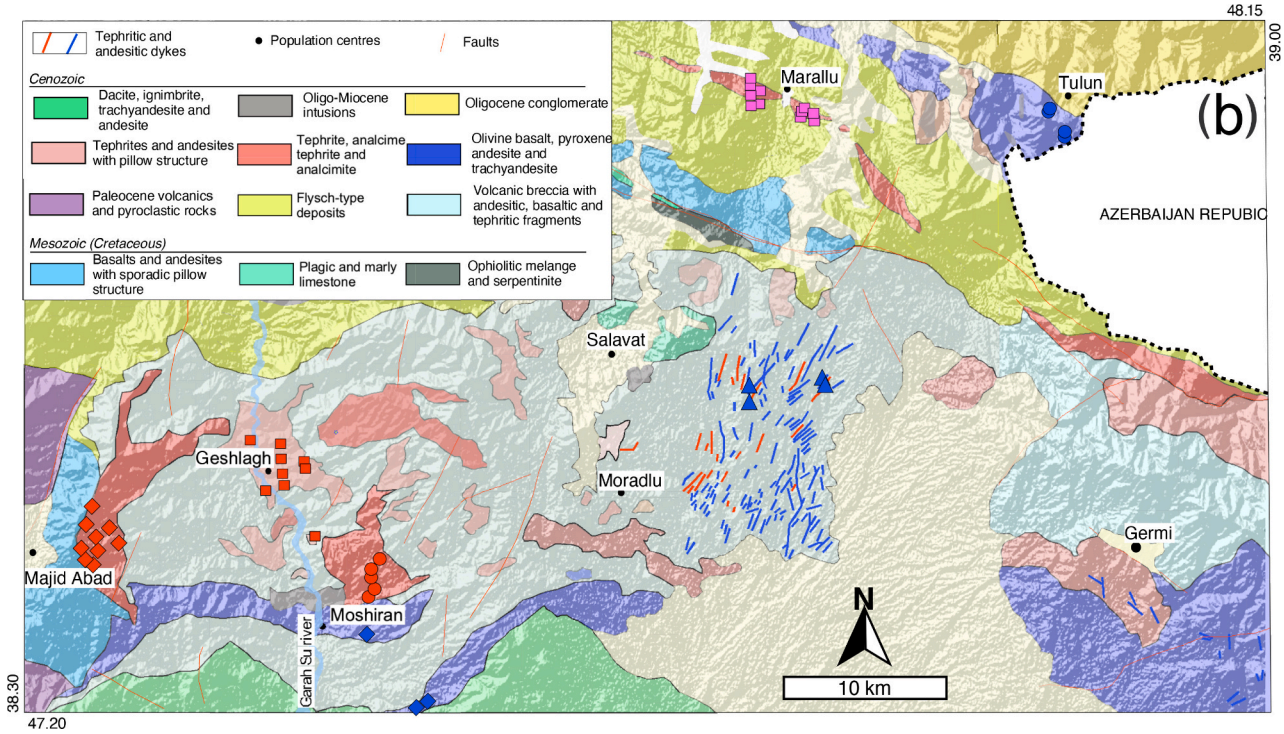

Fig. 1. – (a) Location of the study area and present distribution of Eocene magmatic rocks across southwest Asia (modified from Allen and Armstrong, 2008); (b) Sampling locations of leucite-bearing (Majid Abad, Quarah Su, Moshiran - red symbols) and leucite-free (south Moshiran, Marallu, Tulun, Moradlu - blue symbols) igneous rocks from the Ahar-Arasbaran region (NW Iran). The geological features are taken from the Geological map 1:100,000 published by Geological Survey of Iran (GSI). (For interpretation of the references to colour in this figure legend, the reader is referred to the web version of this article.)

subduction of the Eastern Tauride-South Armenian microcontinent caused slab break-off and opening of asthenospheric window, which, in turn, generated an increase in the heat-flow that triggered melting of the overlying subduction-metasomatised lithospheric mantle (Grosjean et al., 2022 and references therein). The related Eocene calc-alkaline to K-alkaline magmatism developed along a curvilinear belt from Eastern Pontides to peri-Caspian region in northwestern Iran, including the Arasbaran area (Fig. 1a; Dilek et al., 2010). The Geology of the Arasbaran region is mainly composed of Upper Cretaceous-Eocene volcano-sedimentary rocks. Plutonic and volcanic rocks were emplaced starting from the Upper Cretaceous time and continued during the Paleogene until the Quaternary time (Aghazadeh et al., 2011). The Upper Cretaceous–Paleocene marine volcanism includes mafic to intermediate lava flows and pyroclastic rocks with calc-alkaline to high-K calc-alkaline affinities. This period of volcanic activity is also associated with deep-sea marine sediments. Two main Cenozoic volcanic periods are recognized: i) an Eocene volcanic sequence, consisting of potassic trachybasalts, shoshonites, latites, and trachytes, straddling the boundary with more alkali-rich rocks ranging basanites/tephrites, phonolitic tephrites, and phonolites (e.g., Alberti et al., 1980; Dilek et al., 2010; Soltanmohammadi et al., 2018, 2021), which represent the precise focus of this paper; ii) an Upper Miocene-Quaternary sequence having a within-plate geochemical signature, including both basic rocks and differentiated products, that will not be investigated in this paper. Cenozoic plutonic rocks with shoshonitic to ultrapotassic affinity (Aghazadeh et al., 2010, 2011) are also widespread throughout the Ahar-Arasbaran region and the western sector of the Alborz magmatic belt (Castro et al., 2013).

3. Materials and methods

Mafic to intermediate potassic rocks with basaltic to tephritic composition, emplaced in the form of lava flows, pillows, dikes, and pyroclastic units, widely outcrop in the Ahar-Arasbaran region (Fig. 1b). These K-alkaline igneous products are mainly emplaced into deep to shallow level submarine environment, shifting to a subaerial environment along the sequence during the late magmatic stage. The oldest outcrops of potassic igneous rocks in the Arasbaran region are made of pyroclastic units with different thickness, interlayered with silico-clastic sedimentary rocks.

Leucite-bearing volcanic rocks are found in the *Majid Abad, Gheshlagh*, and *Moshiran* areas, whereas leucite- (and foid) free rocks occur in the neighbors of *Moradlu*, *Tulun*, *Marallu* and south of the *Moshiran* villages (Fig. 1b; modified from Geological Survey of Iran-GSI, Geological map 1:100,000). The leucite-bearing lava flows overlie Eocene conglomerates, sandstones and tuffs and are sometimes interlayered with pyrolclastic rocks that are widespread in the *Majid Abad* and *Moshiran* area. Tephritic lava layers (Supplementary Fig. 1a, e) have megaporphyritic to porphyritic texture with centimetric analcime (leucite) phenocrysts. Mafic to intermediate lavas with pillow and columnar jointing structures outcrop in the *Gheshlagh* area (Supplementary Fig. 1c). According to geological maps published by GSI these pillow lavas have andesitic to basaltic composition. The leucite-free rocks outcrop in the form of basaltic and tephritic lava flows interbedded with pyroclastic rocks in the *Tulun* and *south Moshiran* (Supplementary Fig. 1b), and *Marallu* sections (Supplementary Fig. 1f). Trachytic and basaltic dykes, generally with NE-SW direction, outcrop in the *Moradlu* area (Supplementary Fig. 1d).

49 igneous rock samples were collected in order to investigate in extreme detail the volcanic sequence of magmatism of the Ahar-Arasbaran volcanic belt related with the Neotethyan oceanic subduction and collision. Samples were representative of the overall occurrences in the area, and their sampling locations are reported in Fig. 1b. The samples were collected with care to avoid weathered ones, although further care was taken during preparation. Specimens were carefully cut to remove altered portions, and fresh sample aliquots were used to obtain thin sections for petrographic analyses and powders (after grinding in an agate mill) for geochemical analyses.

Major and selected trace elements concentrations (Ni, Co, Cr, V, and Ba) were determined by X-ray fluorescence (XRF) on powder pellets, using a wavelength dispersive automated ARL Advant'X spectrometer at the Dipartimento di Fisica e Scienze della Terra of the University of Ferrara. Accuracy and precision for major elements are estimated as better than 3% for Si, Ti, Fe, Ca, and K, and 7% for Mg, Al, Mn, Na; for trace elements (above 10 ppm) they are better than 10%.

REE, Rb, Sr, Y, Zr, Hf, Nb, Th, and U analyses were carried out, after acid digestion, by inductively coupled mass spectrometry (ICP-MS) at the Dipartimento di Fisica e Scienze della Terra of the University of Ferrara, using a Thermo-Scientific X-Series. Accuracy and precision, based on the replicated analyses of samples and standards, are estimated as better than 10% for all elements, well above the detection limit.

Sample preparation for radiogenic isotope analyses was made at the Dipartimento di Scienze della Terra of the University of Florence. Sample powders were preliminarily leached with 2.5 M HCl for 4 h and then rinsed three times with Milli-Q water. Leaching generally minimize isotopic variation - induced by supergene processes – that may overprint the magmatic signature. Subsequently to leaching, acid digestion by a mixture of HF and HNO_3 was carried out and Sr, Nd and Pb were purified using cation-exchange chromatography. Sr—Nd isotopic ratios were determined at the Dipartimento di Scienze della Terra of the University of Florence using thermal ionization mass spectrometry (Thermo-Fisher Scientific Triton™ Plus) in multi-dynamic mode (e.g., Avanzinelli et al., 2020 and references therein). The normalizing factors used to correct the isotopic fractionation of Sr and Nd were $^{86}Sr/^{88}Sr = 0.1194$, $^{146}Nd/^{144}Nd = 0.7219$ and 0.001% per atomic mass unit, respectively. The within-run $^{87}Sr/^{86}Sr$ average value for NBS 987 reference sample was 0.710253 ± 11 (2σ, $n = 8$), and the $^{143}Nd/^{144}Nd$ average value for the internal standard NdFi was 0.511470 ± 8 (2σ, $n = 6$), identical within error previously published values (Avanzinelli et al., 2020).

Pb radiogenic isotopic analyses were performed using a Thermo Fisher Neptune Plus MC-ICP-MS at the CNR - Istituto di Geoscienze e Georisorse in Pisa (Italy) in 2% HNO_3 solution containing 20–50 ng*g-1 of analyte. The correction for mass bias fractionation of Pb isotope ratios was performed adding an in-house Tl standard to the samples, and isobaric interferences of ^{204}Hg to ^{204}Pb was also corrected. Results were normalized to values recommended by (Todt et al., 1996), respectively 16.9356, 15.4891 and 36.7006 for the $^{206}Pb/^{204}Pb$, $^{207}Pb/^{204}Pb$ and $^{208}Pb/^{204}Pb$ isotope ratios. Full analytical details in Agostini et al. (2022) and in Supplementary Table 1.

K—Ar dating was performed by ActLabs and Geochronex (Ontario, Canada). For Ar analysis, an aliquot of bulk rock powder was weighed, loaded into the sample system of extraction, degassed at ca 100 °C for 2 days to remove the surface gases. Argon was extracted from a double vacuum furnace at 1700 °C and its concentration determined using isotope dilution with ^{38}Ar spike, which is introduced to the sample system prior to each extraction. The extracted gases are cleaned up in a two steps purification process. Then pure Ar is introduced into a magnetic sector mass spectrometer (Reynolds type). Ar isotope ratios were corrected for mass-discrimination and then atmospheric argon was corrected assuming that ^{36}Ar is only from the air. The concentration of radiogenic ^{40}Ar was calculated by using the ^{38}Ar spike concentration. K analysis was performed by ICP.

4. Results

4.1. Petrography

Ahar-Arasbaran igneous rocks were divided in two groups on the basis of the occurrence of leucite, or analcime after leucite, into leucite-bearing and leucite-free, respectively.

4.1.1. Leucite-bearing volcanic rocks

The *Majid Abad* lavas show medium grained, porphyritic to mega porphyritic textures with centimetric leucite, variously transformed in analcime (Fig. 2a), clinopyroxene, plagioclase, and rare sanidine phenocrysts, set in a microcrystalline groundmass composed of the same mineral assemblage plus apatite, opaque minerals and rare glass (Fig. 2b). The *Gheshlagh* pillow lavas show medium grained porphyrytic textures with plagioclase, clinopyroxene, leucite (analcime) and minor iddingsitized olivine as phenoscrysts, in a microcrystalline groundmass of plagioclase, Ti-magnetite, apatite, k-feldspar, foids, other than devitrified glass (Fig. 2c). The columnar jointing lavas have similar petrographic features, but a coarser grained groundmass with respect to that observed in the pillow lavas. Few samples are characterized by abundant olivine and clinopyroxene phenocrysts in a glassy matrix with abundant clinopyroxene microcrystals, recalling the petrographic features of clinopyroxene-rich basaltic andesite (Fig. 2d). The *Moshiran* rocks show petrographic features very similar to the *Majid Abad* lavas, varying from leucite (analcime) porphyry– to –megaporphyritic textures (Fig. 2e) except for the common presence of olivine (altered to iddingsite) and plagioclase as phenocryst phases (Fig. 2f). Most of the leucite-bearing rocks show clear petrographic evidence of cumulus analcime (leucite), except for a couple of columnar jointing lava samples characterized by cumulus clinopyroxene.

4.1.2. Leucite-free rocks

The *Marallu* lavas show medium grained porphyritic texture with clinopyroxene (and rare plagioclase) phenocrysts in a microcrystalline (sometimes glassy) matrix with k-feldspar, plagioclase, clinopyroxene, apatite, biotite and hornblende (Fig. 3a). Clinopyroxene and plagioclase phenocrysts often show sieve textures (Fig. 3b) that, together with replacement of plagioclase and olivine by potassium feldspar and clinopyroxene, suggest that these rocks underwent magma mixing processes. One sample (M-09) shows rare leucite phenocrysts. The *south Moshiran* and *Tulun* lavas have similar petrographic features and are characterized by medium-grained porphyritic textures with olivine, plagioclase and clinopyroxene phenocrysts (Fig. 3c) in an intergranular to intersertal microcrystalline (sometimes containing glass, Fig. 3d) matrix including the same minerals plus apatite and Ti-magnetite. Olivine crystals are often replaced by serpentine and iddingsite, whereas plagioclase and clinopyroxene show sieve texture and compositional zoning. The *Moradlu* hypabyssal rocks show two distinct petrographic features, related to their degree of differentiation. The more mafic rocks are characterized by porphyritic texture with olivine, clinopyroxene and plagioclase phenocrysts in a fine-grained matrix of the same minerals and glass (Fig. 3e). They show petrographic features similar to those of the *south Moshiran* and *Tulun* rocks. The felsic rocks have porphyritic texture with sanidine (and rare plagioclase)

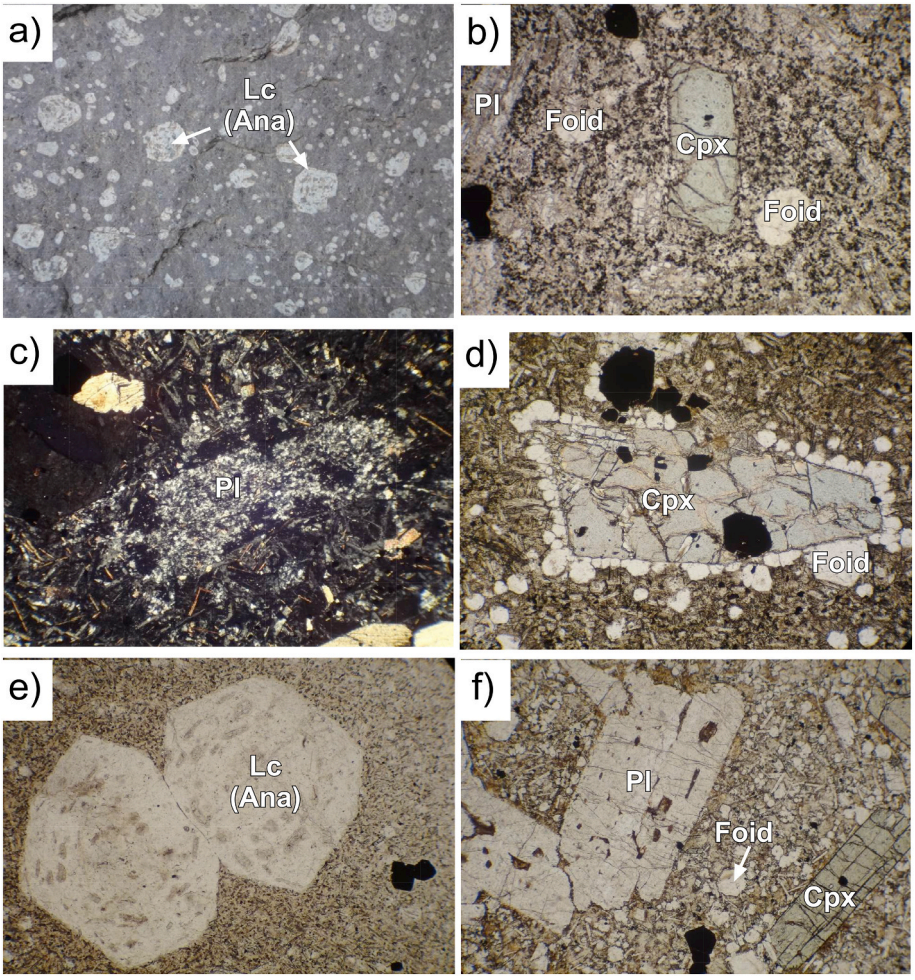

Fig. 2. – Petrographic features of leucite-bearing rocks from the WNW part of the Ahar-Arasbaran region (NW Iran). Lavas from Majid Abad section are characterized by porphyritic to megaporhyritic analcimized leucite (a) and by plagioclase and clinopyroxene phenocrysts in a microcrystalline groundmass (b). Pillow lavas from Quarah Su outcrop show altered plagioclase phenocrysts in a microcrystalline to glassy groundmass (c), whereas columnar jointing lavas contain large clinopyroxene phenocrysts surrounded by abundant foids (d). Lavas from Moshiran show petrographic similarities with those from Majid Abad and are characterized by leucite (deeply analcimized) crystals up to centrimetric in size (e), and the presence of abundant plagioclase phenocrysts (f). Pictures b, d, e, f are taken by optical microscopy in plane polarized light, picture c in crossed polarized light.

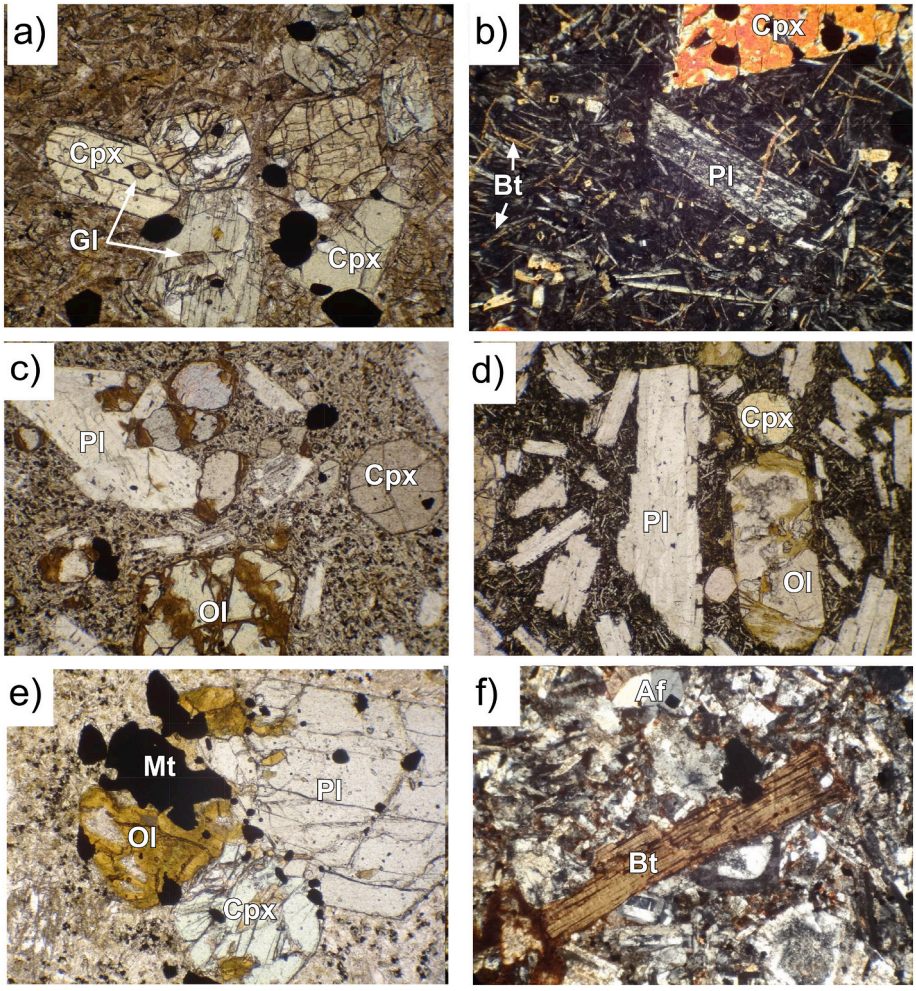

Fig. 3. – Petrographic features and leucite-free rocks from the ESE part of the Ahar-Arasbaran region (NW Iran). Lavas from Marallu outcrop show abundant glomeroporhyritic textures with clinopyroxene phenocrysts, often containing glass (a), and by sieve textured plagioclase and clinopyroxene in biotite-rich matrix (b). Samples from South Moshiran and Tulun outcrops share the same petrographic features, characterized by the presence of olivine, clinopyroxene and plagioclase phenocrysts in a microcrystalline (c) to glassy (d) matrix. Dikes from Moradlu are characterized by mafic to felsic compositions, with the former showing variously iddingsitised olivine, plagioclase and clinopyroxene phenocrysts in a fine-grained olocrystalline matrix composed of the same mineral paragenesis (e), and the latter by the presence of big alkali-feldspars and biotite phenocrysts (f). Pictures b, d, e, f are taken by optical microscopy in plane polarized light, picture c in crossed polarized light.

phenocrysts in the fine to medium grained matrix composed of feldspar, biotite, apatite, opaque minerals, and rare nepheline (Fig. 3f).

4.2. Major and trace element composition

The major and trace element composition of Arasbaran igneous rocks is reported in Supplementary Table 2 and Table 1. The major element budget conforms to that of mafic to intermediate igneous rocks, with SiO_2 varying between 51.5 and 61.7 wt%, and MgO between 7.9 and 0.1 wt%. In the Total Alkali Silica (TAS) diagram (Fig. 4a; Le Maitre et al., 2002), most of the studied samples fall above the divide between sub-alkaline and alkaline series. The leucite-free rocks generally include the least differentiated products of the whole dataset and appear generally less alkaline than leucite-bearing ones, with few samples straddling the alkaline-subalkaline divide. The leucite-bearing rocks include exclusively alkaline rocks, with the exception of 2 clinopyroxene-rich basaltic andesites that show clear cumulus petrographic features.

Among the leucite-bearing rocks the *Majid Abad* section is characterized by shoshonite, latite, tephritic phonolite to phonolite compositions (SiO_2 53.7–58.0 wt%, K_2O 3.5–8.2 wt%), the *Gheshlagh* section by high-K basaltic andesite (2 clinopyroxene -rich samples) to shoshonite, latite and tephritic phonolite (SiO_2 52.4–54.2 wt%, K_2O 2.3–6.6 wt%), and the *Moshiran* section varies from latite to tephritic phonolite (SiO_2 54.8–55.2 wt%, K_2O 1.3–5.1 wt%).

Among the leucite-free rocks, samples from the *Marallu* section plot at the boundary between shoshonite, latite, phonolitc tephrite and tephritic phonolite fields (SiO_2 53.2–54.3 wt%, K_2O 4.5–7.2 wt%), whereas those from the *Tulun* and *south Moshiran* sections in the shoshonite field (SiO_2 51.9–54.0 wt%, K_2O 3.0–4.9 wt%). Mafic and felsic dikes outcropping westward from *Moradlu* are shoshonitic (SiO_2 51.5–53.7 wt%, K_2O 4.2–6.3 wt%) to trachytic (SiO_2 61.5–61.7 wt%, K_2O 6.3 wt%) in composition.

Despite of the above cited differences between the two lithotypes, according to the K_2O vs SiO_2 classification diagram (Peccerillo and Taylor, 1976; Fig. 4b) all the studied Arasbaran igneous rocks display shoshonitic affinity except for the clinopyroxene-rich basaltic andesites. However, the normative composition reveals that leucite-bearing rocks are more silica-undersaturated than leucite-free ones (Fig. 5).

The Ahar-Arasbaran rocks are characterized by a variable Loss on Ignition (LOI) values, ranging between 0.6 and 6.7 wt% and displaying a broad inverse correlation with CaO; leucite-bearing rocks show relatively high LOI values due to the presence of low-temperature secondary phases (e.g., analcime from leucite and calcite). In any case, the restricted compositional range observed for an element scarcely mobile

Table 1
– Bulk rock trace (incompatible and REE) elements composition of representative Eocene Ahar-Arasbaran igneous rocks obtained by inductively coupled plasma mass spectrometry (ICP-MS). Sample characteristics and abbreviations as in Supplementary Table 2.

Sample	M-04}	M-06}	M-12}	M-14}	M-15}	M-17}	M-21}	M-26}	M-27}	M-29}	M-32}	M-33}	M-36}	M-38}	M-40}	M-45}	M-51}	M-54}	M-56}	M-58}	M-60}
Lithology	Lava	Lava	Lava	Lava	Dike	Dike	Lava	Lava	Lava	Lava	Pillow	Pillow	Columnar lava flow	Pillow	Pillow	Pillow	Lava	Lava	Lava	Lava	Lava
Rock-type	**Lc-free**	**Lc-free**	**Lc-free**	**Lc-free**			**Lc-bearing**	**Lc-bearing**	**Lc-bearing**	**Lc-bearing**	**Lc-bearing**	**Lc-bearing**	**Lc-bearing**	**Lc-bearing**	**Lc-bearing**	**Lc-bearing**	**Lc-bearing**	**Lc-free**	**Lc-free**	**Lc-free**	**Lc-free**
Classification	Tr-And.	Tr-And.	Tr-And.	Tr-And.	Trachite	Bas. Tr-And.	Tr-And.	Tr-And.	Tr-And.	Tr-And.	Tr-And.	Tr-And.	Tr-And.	Tr-And.	Bas.And.*	Tr-And.	Tr-And.	Bas. Tr-And.	Bas. Tr-And.	Bas. Tr-And.	Bas. Tr-And.
Locality	Marallu	Marallu	Marallu	Marallu	Moradlu	Moradlu	Majid Abad	Majid Abad	Majid Abad	Majid Abad	Gheshlagh	Gheshlagh	Gheshlagh	Gheshlagh	Gheshlagh	Gheshlagh	Moshiran	S. Moshiran	S. Moshiran	Tulun	Tulun
Rb (ppm)	71.8	71.3	55.2	88.1	156	41.3	102.6	119.0	37.0	144.1	56.5	44.2	91.2	48.6	44.6	42.7	87.4	73.3	39.4	51.6	74.3
Sr	1747	1547	913	1314	262	520	1802	1914	1594	2152	848	701	957	518	2932	1594	1736	477	666	466	509
Y	17.9	19.6	17.9	16.9	16.2	13.5	23.4	17.2	18.3	20.1	15.8	14.8	18.7	12.0	15.2	15.8	18.1	22.0	18.9	17.2	21.7
Zr	140	143	139	147	430	85	152	127	154	168	92	99	94	97	65	99	149	216	126	123	191
Nb	13.4	13.3	13.2	13.5	58.4	6.8	16.2	13.4	14.6	20.8	7.2	7.6	7.3	7.5	4.2	9.0	18.4	22.5	15.9	15.0	23.4
La	40.0	41.3	39.1	39.3	36.1	13.7	52.9	38.8	37.3	48.4	27.4	25.7	33.2	21.5	16.8	23.2	35.6	31.7	23.7	23.0	29.7
Ce	74.9	77.1	73.1	75.4	76.8	29.8	74.5	61.3	78.3	69.8	46.4	45.6	55.1	45.8	30.7	40.4	63.8	60.8	46.0	44.3	55.4
Pr	8.22	8.56	8.09	8.16	6.99	3.44	8.81	6.62	8.11	8.24	5.35	5.15	6.28	4.47	3.87	4.67	6.83	6.75	5.31	5.11	6.37
Nd	32.9	33.9	32.5	32.6	24.7	14.8	32.7	24.6	33.5	30.2	21.4	20.6	24.7	18.0	17.1	18.6	27.1	26.7	21.9	20.8	25.5
Sm	6.17	6.49	6.15	6.22	4.28	3.33	5.94	4.48	6.59	5.47	4.15	4.02	4.69	3.54	3.72	3.62	5.10	5.07	4.35	4.22	4.93
Eu	1.72	1.80	1.71	1.73	0.69	1.04	2.09	1.55	2.02	1.88	1.49	1.45	1.69	1.27	1.47	1.53	1.90	1.30	1.36	1.26	1.44
Gd	5.66	5.94	5.61	5.65	4.10	3.27	5.73	4.38	6.16	5.16	3.97	3.88	4.59	3.46	3.85	3.96	5.68	5.56	4.78	4.37	5.34
Tb	0.78	0.82	0.78	0.78	0.61	0.54	0.81	0.61	0.86	0.73	0.58	0.56	0.66	0.50	0.55	0.55	0.72	0.77	0.68	0.64	0.75
Dy	3.54	3.80	3.60	3.52	3.02	2.82	3.78	2.91	3.93	3.38	2.79	2.72	3.13	2.40	2.74	2.63	3.23	3.83	3.32	3.02	3.70
Ho	0.70	0.75	0.70	0.70	0.65	0.59	0.77	0.59	0.76	0.68	0.58	0.56	0.64	0.49	0.54	0.54	0.65	0.79	0.69	0.62	0.76
Er	1.88	2.01	1.91	1.87	1.92	1.58	2.15	1.67	2.00	1.91	1.63	1.60	1.80	1.39	1.46	1.51	1.81	2.18	1.87	1.67	2.12
Tm	0.30	0.33	0.31	0.30	0.35	0.26	0.37	0.28	0.31	0.32	0.27	0.27	0.30	0.23	0.26	0.28	0.32	0.38	0.35	0.30	0.37
Yb	1.77	1.89	1.76	1.74	2.12	1.48	2.18	1.70	1.84	1.95	1.66	1.61	1.82	1.42	1.45	1.56	1.78	2.19	1.81	1.68	2.06
Lu	0.27	0.29	0.28	0.26	0.34	0.23	0.34	0.26	0.28	0.31	0.26	0.25	0.28	0.22	0.22	0.25	0.28	0.35	0.27	0.26	0.32
Hf	3.40	3.48	3.46	3.58	9.71	2.38	3.33	2.82	3.86	3.46	2.30	2.43	2.33	2.42	1.75	2.32	3.14	4.98	3.03	2.90	4.12
Ta	0.58	0.58	0.56	0.58	2.34	0.32	0.67	0.55	0.62	0.82	0.36	0.37	0.37	0.36	0.28	0.50	0.80	1.04	0.75	0.70	1.07
Th	10.0	10.6	9.7	9.6	20.6	3.4	13.1	10.0	7.6	13.5	6.8	6.8	7.3	6.0	4.8	7.8	12.1	14.9	5.8	6.1	11.4
U	2.69	2.73	2.58	2.70	6.09	1.10	2.50	1.86	2.01	3.04	2.49	1.66	1.92	1.20	1.32	2.02	3.18	3.56	1.43	1.54	2.81

* = cpx-rich.

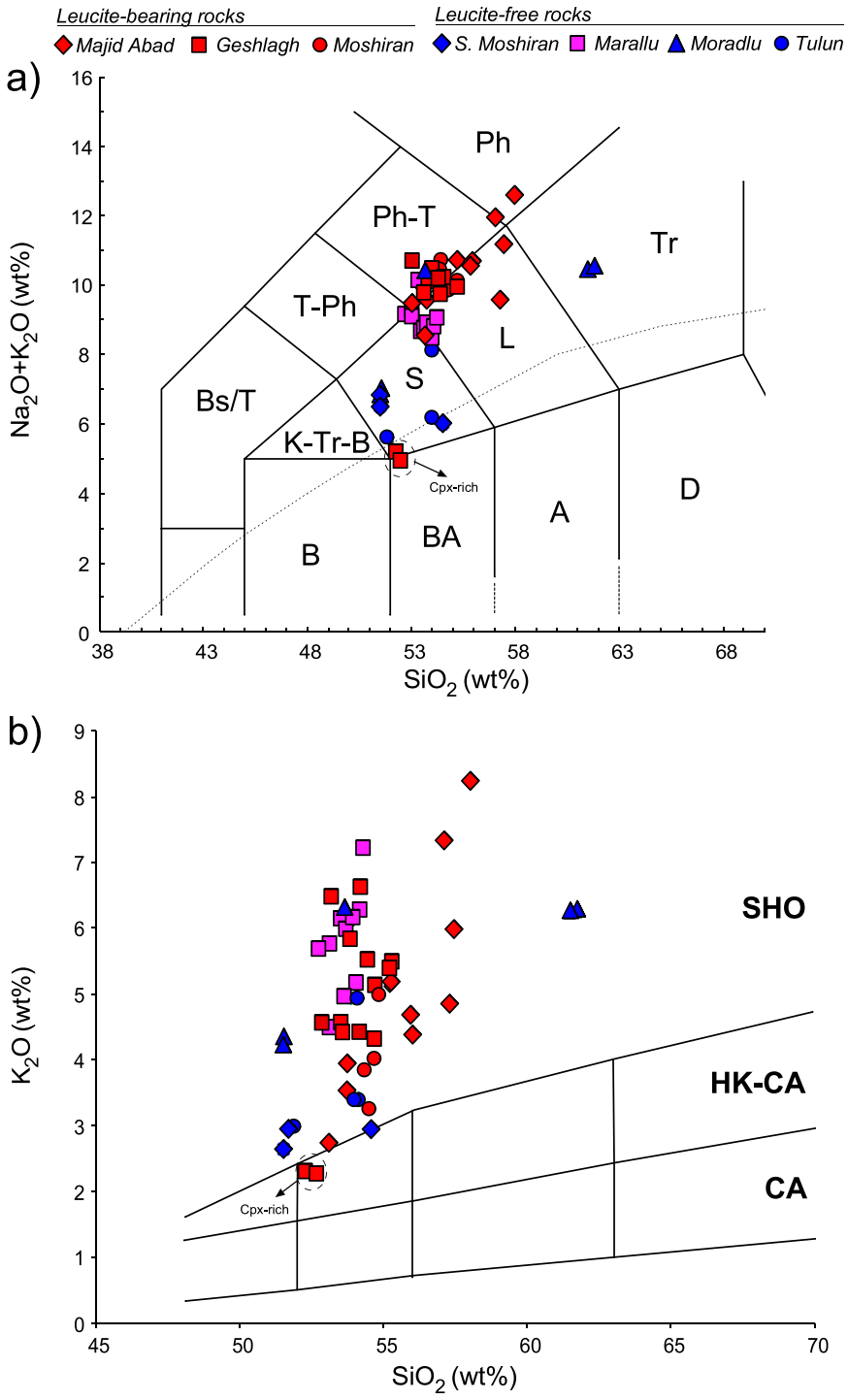

Fig. 4. – (a) TAS (Le Maitre et al., 2002) and (b) K_2O vs SiO_2 (Peccerillo and Taylor, 1976) classification diagrams of leucite-bearing and leucite-free igneous rocks from the Ahar-Arasbaran region (NW Iran). B = basalt, BA = basaltic andesite, A = andesite, D = dacite, K-Tr-B = potassic trachybasalt, S = shoshonite, L = latite, Tr = trachyte, Bs/T = basanite/tephrite, Ph-T = phonolitic tephrite, T-Ph = tephritic phonolite, Ph = phonolite, CA = calcalkaline series, HK-CA = high-K calcalkaline series, SHO = shoshonite series.

during weathering processes such as TiO_2, and the lack of clear relationships between LOI and major oxides (with the exception of CaO) suggest that the bulk rock major element composition (recalculated on anhydrous basis) still preserves information on the magmatic signature.

The variation diagrams of figure 6 show that MgO is inversely correlated with SiO_2, Al_2O_3, alkalis (Na_2O and K_2O, not shown), and directly correlated with Fe_2O_3 and TiO_2, consistent with different degrees of fractional crystallization. All the investigated volcanic products depict a common distribution, with the exception of the *Gheshlagh* pillow lavas, which are characterized by invariably lower TiO_2, Fe_2O_3, CaO, higher alkalis and Al_2O_3 contents at comparable MgO. The main difference in the liquid lines of descent (LLD) of leucite-bearing and leucite-free rocks is represented by the variation of CaO and Al_2O_3 of the least differentiated products, with the former characterized by a higher clinopyroxene fractionation with respect to the latter (Supplementary Fig. 2). Leucite-bearing *Gheshlagh* pillow lavas show the lowest compatible trace elements content, coupled with a distinctive enrichment in the most incompatible Large Ion Lithophile Element (LILE) such

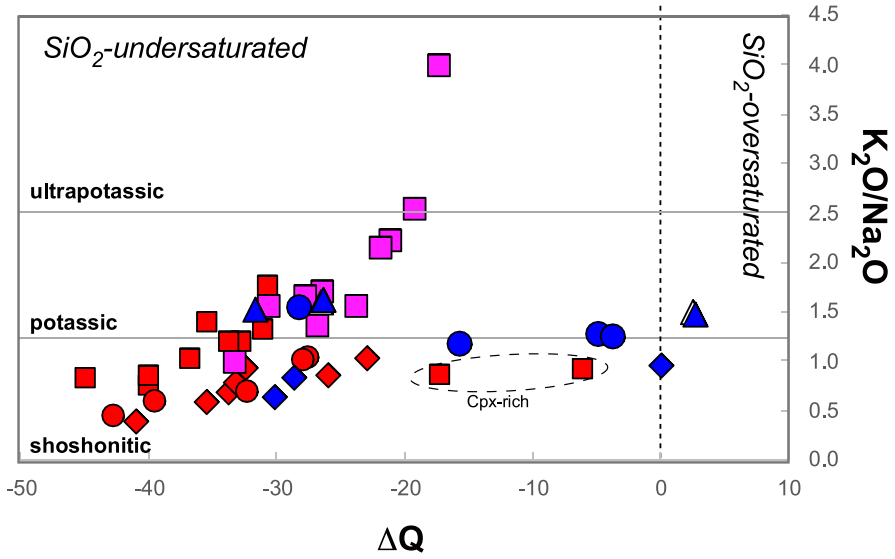

Fig. 5. – Δq vs K_2O diagrams showing the different silica-saturation conditions of leucite-bearing and leucite-free igneous rocks from the Ahar-Arasbaran region (NW Iran). Symbols as in Fig. 4.

as Ba (Fig. 6g). On the other hand, the leucite-free rocks (*South Moshiran, Tulun* lavas and *Moradlu* dykes) show a relative enrichment in High-Field Strength Elements (HFSE), as demonstrated by the distribution of Zr and Nb (Fig. 6f and h).

Primitive Mantle (PM)-normalized incompatible element distribution (Fig. 7) of Arasbaran igneous rocks show the typical features of subduction-related magmatism, with troughs in HFSE (Nb, Ta, Ti, Zr) and spikes in LILE (Ba and K) and Pb. Coherently, in the Ce/Yb vs Ta/Yb and diagram (Fig. 8a) proposed by Pearce (1982) Arasbaran rocks plot in the shoshonite field. This affinity, certainly attributable to a convergent plate setting, is confirmed by the use of recent tectonomagmatic diagrams (Fig. 8b and c) such as those proposed by Hastie et al. (2007) and Saccani (2015).

Notably, leucite-bearing rocks are generally characterized by a higher LILE/HFSE ratio, with respect to leucite-free ones. In particular, samples from *Majid Abad*, *Gheshlagh* and *Moshiran* show average Ba/Nb of 157, 242 and 106, respectively, whilst samples from *South Moshiran, Tulun* and *Marallu* generally show lower average ratios (43, 63 and 98, respectively). Similar distribution concerns the LILE/REE ratio, which shows distinct ranges for leucite-bearing rocks (Ba/La 30–117) and leucite-free rocks (Ba/La 10–32). These geochemical features are also observed in other Late-Cretaceous-Eocene leucite-bearing and leucite-free rocks from NW Iran (Lahrud: Shafaii Moghadam et al., 2018; Moghan: Amraee et al., 2019), Central (Gülmez et al., 2016) and Eastern Pontides (Altherr et al., 2008; Eyuboglu et al., 2011). Leucite-free and leucite-bearing rocks are characterized by overlapping REE patterns, with La_N/Yb_N varying from 6.3 to 17.8, which is inversely correlated with MgO (wt%), probably as a result of fractional crystallization of clinopyroxene in the most evolved products. Striking differences are also observed in the Eu/Eu* values, which are systematically higher in the leucite-bearing rocks (1.05–1.15) with respect to leucite-free rocks (0.82–0.88).

4.3. Sr-Nd-Pb isotopic composition

The Sr and Nd isotopic compositions of the Arasbaran rocks plot between the depleted MORB mantle (DM) and enriched mantle components (Fig. 9). On the whole, the $^{87}Sr/^{86}Sr_{(i)}$ varies between 0.704407 and 0.705669, whereas $^{143}Nd/^{144}Nd_{(i)}$ values range from 0.512572 to 0.512791 (Table 2). Notably, leucite-bearing rocks are characterized by the lowest Sr and the highest Nd radiogenic values plotting above the Bulk Silicate Earth (BSE), whilst leucite-free ones display more radiogenic Sr and less radiogenic Nd compositions, with the *Moradlu* mafic and felsic dykes showing the most radiogenic Sr values. The lead isotopic composition of the Arasbaran igneous rocks is reported in (Fig. 10a). All samples are characterized by lead isotope values well above the Northern Hemisphere Reference Line (NHRL - Hart, 1984) on $^{207}Pb/^{204}Pb$ vs $^{206}Pb/^{204}Pb$ and $^{208}Pb/^{204}Pb$ vs $^{206}Pb/^{204}Pb$ (not shown). They vary from 18.60 to 18.75 for $^{206}Pb/^{204}Pb$, from 15.58 to 15.64 for $^{207}Pb/^{204}Pb$ and from 38.69 to 38.87 for $^{208}Pb/^{204}Pb$. It is noteworthy that the leucite-bearing rocks are characterized by the lowest Pb radiogenic values ($^{206}Pb/^{204}Pb$ 18.58–18.65, $^{207}Pb/^{204}Pb$ 15.57–15.60, $^{208}Pb/^{204}Pb$ 38.63–38.71), whereas the leucite-free rocks the highest Pb radiogenic composition ($^{206}Pb/^{204}Pb$ 18.65–18.75, $^{207}Pb/^{204}Pb$ 15.61–15.64, $^{208}Pb/^{204}Pb$ 38.65–38.87), thus defining distinct Pb compositional features.

4.4. K—Ar dating

K—Ar radiometric ages have been carried out on 6 samples representative of the various leucite-free and leucite-bearing Arasbaran igneous rocks (Table 2). Although K—Ar dating indicates that all the investigated samples are nearly coeval and of Middle Eocene in age (Lutetian-Bartonian), slight but significant differences can be observed. Leucite-free rocks were mainly emplaced from 41.9 +/− 1.1 Ma at *South Moshiran* to 40.0 +/− 1.1 Ma at *Marallu*, whereas leucite-bearing lavas are slightly younger and were erupted in a short time interval from 39.6 +/− 1.0 at *Majid Abad* to 39.4 +/− 1.0 Ma at *Gheshlagh*.

5. Discussion

The main petrographic, geochemical and isotopic features of the Arasbaran igneous rocks are discussed below in order to define the magmatic affinities, the space-time distribution of the different magma types and the nature of the metasomatic agents affecting their mantle sources, in turn related the subduction geodynamic framework in this sector of the Alpine-Himalayan belt.

5.1. Magmatic affinity and differentiation processes of the Arasbaran volcanic rocks

The observed mineralogical paragenesis and the related geochemical features of the Ahar-Arasbaran igneous products are important markers indicating that the relative magmas were mafic and potassic, similar to

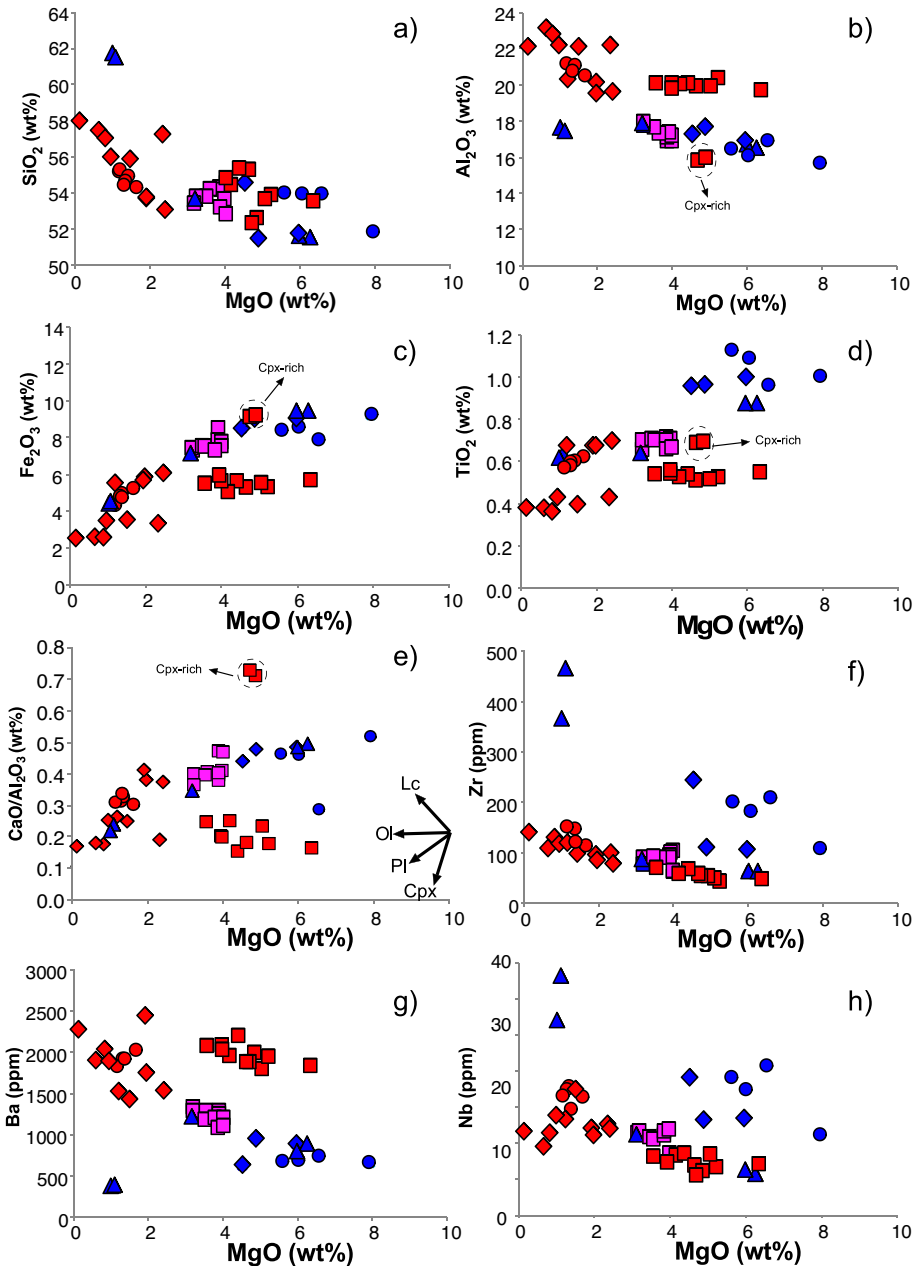

Fig. 6. – Major element versus MgO (wt%) bivariate diagrams of leucite-bearing and leucite-free igneous rocks from Arasbaran area (NW Iran). Symbols as in Fig. 4.

what observed in many Cenozoic "orogenic" (subduction-related) volcanic rock associations of the circum-Mediterranean area (Beccaluva et al., 2013; Bianchini et al., 2008; Conticelli et al., 2009, 2015). Petrographic observation allows distinguishing two different rock-types zonally arranged in adjacent sectors of the study area: leucite (analcime)-bearing rocks at *Majid Abad, Gheshlagh* and *Moshiran* (WNW) and leucite (analcime)-free rocks occurring at *South Moshiran, Marallu, Tulun* and *Moradlu* (ESE). The genesis of analcime in silica-undersaturated rocks is highly debated, since it can occur either as primary magmatic crystallizing phase or by secondary post-magmatic/hydrothermal substitution over leucite (e.g., Luhr and Kyser, 1989). Despite the primary genesis of analcime bearing rocks in this sector of the Alpine-Himalayan belt has been proposed by Soltanmohammadi et al. (2021), petrographic observation and data support better a secondary origin according to several other authors (e.g., Altherr et al., 2008; Amraee et al., 2019; Comin-Chiaramonti et al., 1979; Eyuboglu et al., 2011). Indeed, primary analcime should be also characterized by low K and high Fe contents, which is not observed. The low Fe contents of analcime in NW Iran (Soltanmohammadi et al., 2021) and the absence of magmatic hydrous minerals such as amphibole or mica argues for a secondary origin for analcime in the studied rocks as a product of leucite transformation.

Noteworthy, the petrographic differences of the two lithotypes reflect different water content and degrees of silica-undersaturation. Leucite-bearing rocks are generally water-free and are characterized by lower silica saturation index (Δq = CIPW normative $q - [lc + ne + kal + ol]$) and K_2O/Na_2O, with respect to leucite-free rocks (Fig. 5). The lack of high K_2O/Na_2O terms among leucite-bearing rocks is probably related to the effect of weathering, with the preferential loss of K_2O over Na_2O. As reported by Prelević et al. (2004), analcimization and alteration mainly induce loss of K_2O and Rb, suggesting that the protolith of leucite-bearing rocks were highly potassic. The same interpretation was provided by Altherr et al. (2008) for plagioleucitites from the Pontides,

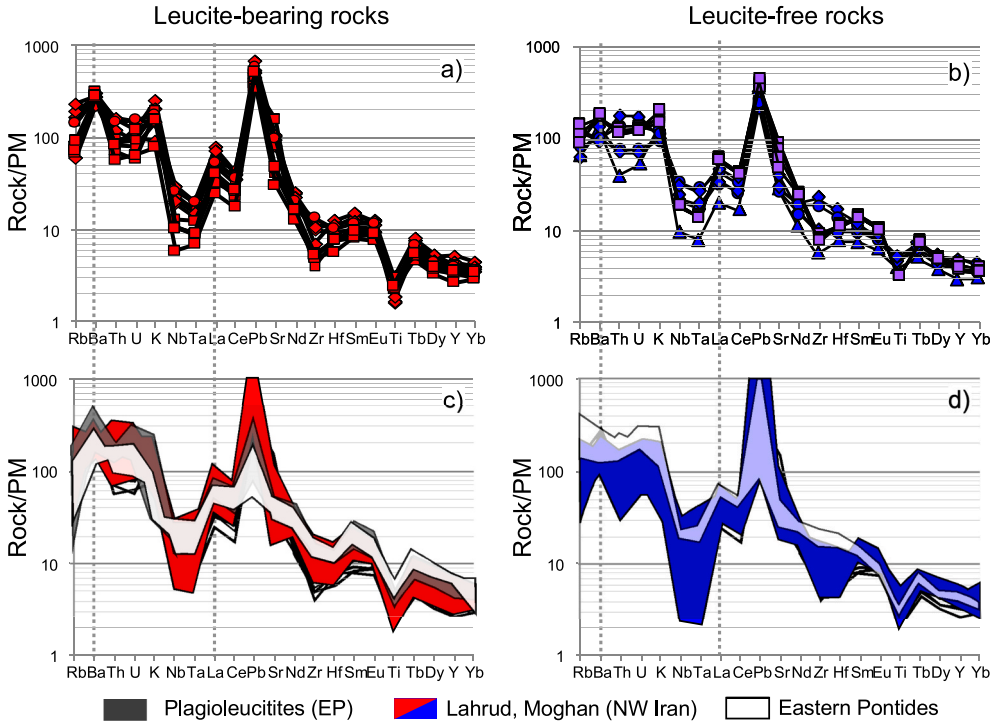

Fig. 7. – Primitive Mantle (PM)-normalized incompatible element patterns of leucite-bearing (a) and leucite-free (b) igneous rocks from the Ahar-Arasbaran region (NW Iran). The distribution of nearly coeval leucite-bearing (c) and leucite-free (d) rocks from NW Iran (Lahrud – Shafaii Moghadam et al., 2018; Moghan – Amraee et al., 2019) and from Eastern Pontides (Altherr et al., 2008; Eyuboglu et al., 2011) are also reported for comparison. Normalizing factors are from Sun and McDonough (1989). Symbols as in Fig. 4.

who suggested an ultrapotassic affinity for these rocks.

Leucite-bearing *Gheshlagh* lavas include the most mafic end-members observed in the region (mg# 0.57–0.70) and do not show petrographic evidence of extra olivine accumulation, thus representing the most suitable candidates as the parental melts of this magma type. These rocks are, however, characterized by variable Na_2O/K_2O, high Al_2O_3 and LOI confirming the petrographic evidence of leucite accumulation and analcime formation after leucite during weathering. Their low CaO (and Sc) at relatively high MgO and Al_2O_3 contents indicates that they suffered anyway significant clinopyroxene fractionation. We recalculated the original composition of the parental leucite-bearing magmas starting from the most mafic and potassic samples (samples M31, M36, M39). We backward corrected their geochemical composition for the pseudomorphic substitution of analcime (from 10 to 25 vol%) over leucite (mineral chemistry from Comin-Chiaramonti et al., 2009), and we accounted for a fractionated paragenesis based on the petrographic observation (i.e., addition of 10–20% clinopyroxene, mineral chemistry from Conticelli et al., 1997). The reconstructed parental compositions comply with the geochemical criteria defined by Foley et al. (1987) for the classification of ultrapotassic rocks (i.e., MgO and $K_2O > 3$ wt%, $K_2O/Na_2O > 2$). When plotted in the Foley's classification diagrams (Supplementary Fig. 3), the recalculated magmas fall in "Roman Type" field, together with the leucitites and plagioleucitites of both the Italian Roman province (data compilation from Conticelli et al., 2015) and the Central and Eastern Pontides (Altherr et al., 2008; Gülmez et al., 2016).

Contrarily, the *South Moshiran*, *Moradlu* and *Tulun* leucite-free rocks do not show evidence of significant fractionation and alteration processes. They have too low K_2O/Na_2O (< 1.5) to be considered ultrapotassic, displaying instead a shoshonitic affinity. The *Marallu* lavas show intermediate geochemical features between leucite-bearing and leucite-free rocks (K_2O/Na_2O between 1.0 and 4.0).

In order to test the possible occurrence of magmatic relationships among the Arasbaran rocks suites the thermodynamically based Magma Chamber Simulator model (MSC, Bohrson et al., 2020) for fractional crystallization processes (FC) has been applied to leucite-bearing and leucite-free magma types. Leucite-bearing rocks type are characterized by a wide spectrum of volcanic products at increasing differentiation degree from the *Gheshlagh* pillow and columnar jointing lavas (mg# up to 0.7) to the *Majid Abad* lavas (mg# down to 0.1). The observed small, but significant differences in the isotopic composition would also suggest a distinct mantle source for the mafic and intermediate/felsic leucite-bearing products. However, these products share petrographic and geochemical similarities, suggesting that they are nearly comagmatic. We thus tested if the most differentiated leucite-bearing products can be achieved through a simple FC model. Starting from the backward corrected composition of the *Gheshlagh* mafic lavas, the FC trend of the leucite-bearing rocks (FC1) correctly reproduce the observed major elements distribution of the more differentiated products, confirming their common magmatic affinity (Supplementary Fig. 2). The results show that the most differentiated leucite-bearing products are compatible with fractionation of 10–16% Ol, 20–40% Pl, 10–20% Cpx, 5–15% Leu, 2–10% Af and 4–5% Fe—Ti oxides, from the relative calculated parental magmas, at the pressure of 1 Kb, oxygen fugacity on QFM buffer with low (0.5–1.0 wt%) initial water content. The liquid fraction corresponding to the most differentiated leucite-bearing product vary from 20 to 25% of the original parental melt at the temperature of 850 °C. The fractionated mineralogy and the crystallization order is consistent with that observed by petrographic analysis of the most differentiated leucite-bearing samples. In particular, the occurrence of leucite on the liquidus after clinopyroxene and plagioclase, and its rapid growth predicted by the model, is compatible with what observed in megaporphyritic samples showing big leucite crystals including the above cited mineral phases having higher crystallization temperature. The selected initial water content of parental magma is an important variable (at isobaric conditions) for reproducing the observed crystallization order and mineral proportions of the leucite-bearing melts. Indeed, at low initial water content (ca. 0.5 wt% H_2O) the model predicts an early appearance of leucite on the liquidus following olivine in the crystallization

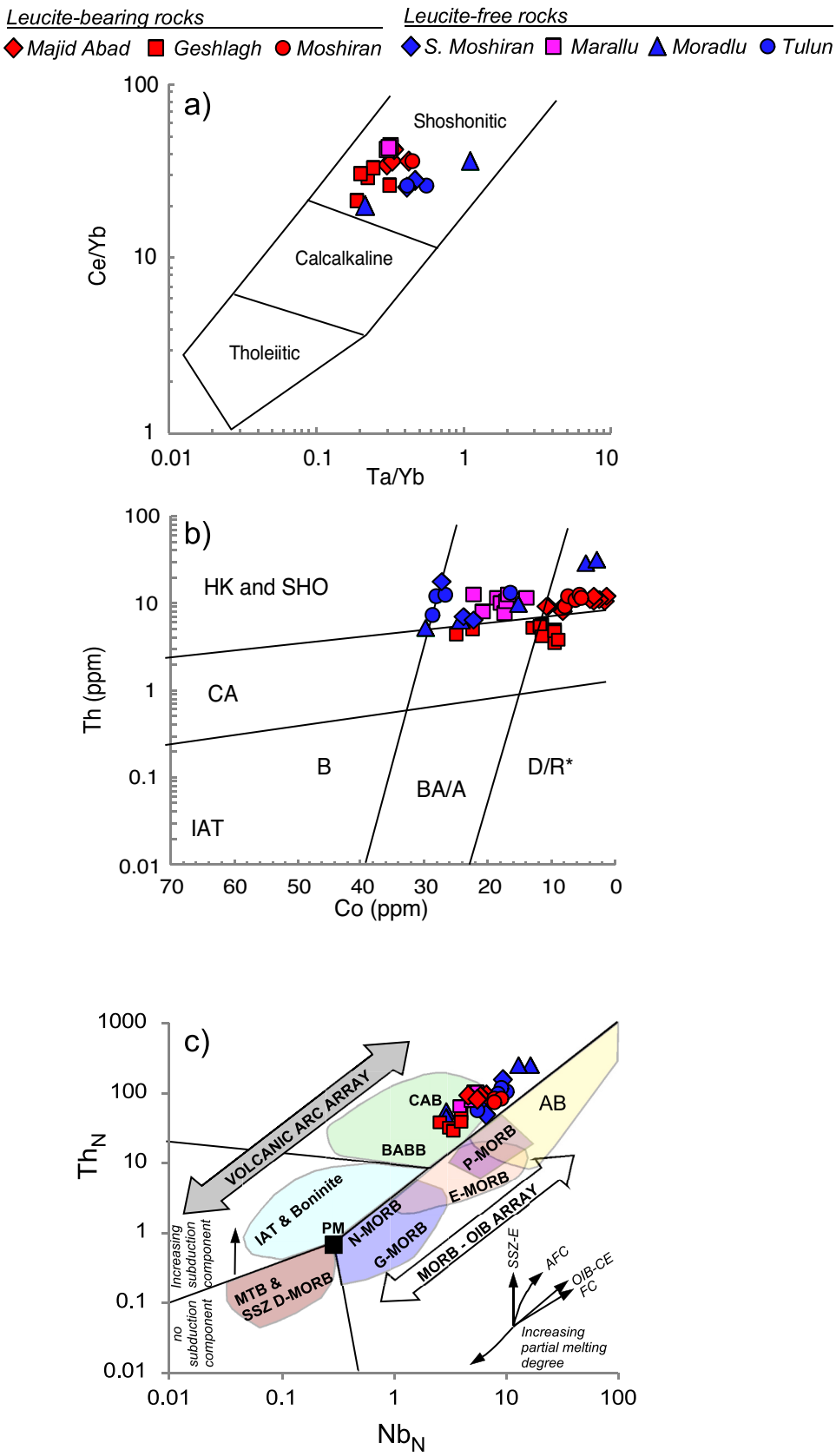

Fig. 8. – Trace element discrimination diagrams for leucite-bearing and leucite-free igneous rocks from the Ahar-Arasbaran region (NW Iran). a) Ce/Yb vs Ta/Yb (Pearce, 1982), b) Th vs Co (Hastie et al., 2007) for altered rocks and c) N-MORB normalized Th vs Nb (Saccani, 2015).

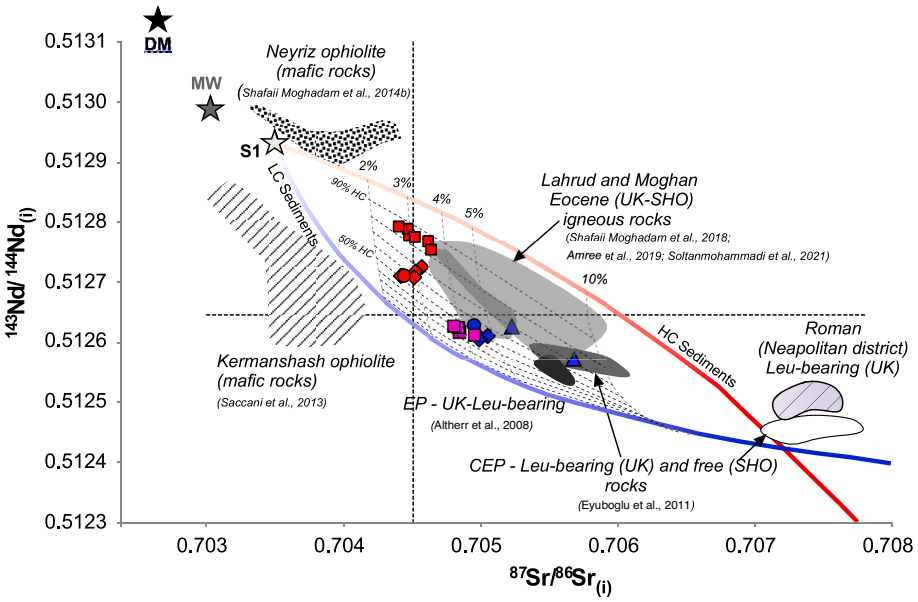

Fig. 9. – Initial Sr—Nd isotope ratios of leucite-bearing and leucite-free igneous rocks from the Ahar-Arasbaran region (NW Iran). The distribution of nearly coeval leucite-bearing and leucite-free rocks from NW Iran (Lahrud – Shafaii Moghadam et al., 2018; Moghan – Amraee et al., 2019) and from Eastern Pontides (Altherr et al., 2008; Eyuboglu et al., 2011) are also reported for comparison. S1 is the composition of the mantle wedge (MW; Sr = 22 ppm, $^{87}Sr/^{86}Sr = 0.70298$, Nd = 0.3 ppm, $^{143}Nd/^{144}Nd = 0.51299$) after the first metasomatic events obtained by the addition of 6% of slab partial melts (Sr = 630 ppm, $^{87}Sr/^{86}Sr = 0.70393$, Nd = 3.0 ppm, $^{143}Nd/^{144}Nd = 0.51273$) of Zagros Neotethyan MORB ophiolites as AOC (Saccani et al., 2013; Shafaii Moghadam et al., 2014). The blue and red mixing lines represents the second metasomatic events characterized by the addition of low-carbonate (LC) and high-carbonate (HC) sediment melts to the S1 mantle source, respectively. The composition of AOC partial melts and those of HC (Apennine marl SD48 – Avanzinelli et al., 2018; Sr = 519 ppm, $^{87}Sr/^{86}Sr = 0.70822$, Nd = 2.8 ppm, $^{143}Nd/^{144}Nd = 0.512163$) and LC (average Mariana pelagic clays 800 and 801 – Plank and Langmuir, 1998; Sr = 355 ppm, $^{87}Sr/^{86}Sr = 0.71055$, Nd = 22 ppm, $^{143}Nd/^{144}Nd = 0.51235$) sediments partial melts were obtained using bulk/melt ratios from the experimental work of Carter et al. (2015) for AOC, and Skora et al. (2015) for HC and LC, at temperatures between 900 and 1000 °C. Dashed lines represents tie lines linking the same proportions of HC and LC sediment melt component. Symbols as in Fig. 4. (For interpretation of the references to colour in this figure legend, the reader is referred to the web version of this article.)

sequence, whereas at higher water magma initial content (> 1.0 wt% H_2O) leucite is not present in the fractionated solid assemblage and potassium is mainly hosted by alkali feldspar and minor biotite. The low water content of the parental leucite-bearing rocks was also inferred for Central Pontides (Gülmez et al., 2016) and for the Roman (Avanzinelli et al., 2009; Conticelli et al., 2015) rocks, and it is in agreement with the favored conditions for leucite crystallization in low P_{H2O} conditions (Freda et al., 1997). Therefore, the model results suggested that the physico-chemical conditions of differentiation for the leucite-bearing magma that best fit the petrographic features and the LLD of this suite include a FC process at low (1.0 Kb) pressure and a low water content of the parental magma ranging from 0.5 to 1.0 wt%.

The same FC modelling has been applied to leucite-free samples, using the most mafic samples (M58, M56 and M17 for the *South Moshiran, Tulun* and *Moradlu* series, respectively – black asterisk symbols in Supplementary Fig. 2) as parental melts. The composition of the most differentiated products of the leucite-free rocks, identified by the *Moradlu* trachytic dikes, can be successfully matched by the FC crystallization trends (FC2) of the related parental melts with 1.0–1.5 wt% water content at the pressure of 1 Kb and at QFM oxygen fugacity buffer (Supplementary Fig. 2). In particular, the fractionation of 9–13% Ol, 12–17% Cpx, 23–33% Pl, 5–6% Fe—Ti oxides and 0.5% Ap from the most mafic leucite-free melts allow reproducing the composition of the most differentiated products, which correspond to a liquid fraction of ca. 40% of the parental melt at ca. 1000 °C. The higher volatile content of the leucite-free rocks is confirmed by the significant presence of biotite in the mineral paragenesis, which is also predicted by the model. The *Marallu* series, although lacking petrographic evidence of leucite in its mineral assemblage, often plot in between the FC1 and FC2 differentiation trends, suggesting a possible derivation by a mixing of the two main magma types of the Arasbaran area. This is corroborated by the pervasive sieved textures observed in their phenocrysts (Fig. 4), by the intermediate isotopic composition (Fig. 9), as well as by the geographic position in between of the leucite-bearing and leucite-free occurrences (Fig. 1b).

5.2. *Magma genesis, metasomatic agents and mantle sources of the Arasbaran rocks*

The geochemical features of both leucite-free and leucite-bearing rocks conform to those of magma series typically occurring at destructive plate margins in connection with subduction and subsequent collisional processes (e.g., Beccaluva et al., 2013; Conticelli et al., 2009, 2015; Conticelli and Peccerillo, 1992 and references therein). In fact, the incompatible element distribution of all the Arasbaran igneous rocks show the typical features of subduction-related magmatism, with troughs in Nb–Ta-Ti-Zr (HFSE) and spikes in Ba—K (LILE) and Pb. However, leucite-bearing rocks are characterized by higher LILE/HFSE (e.g., Ba/Nb), LILE/LREE (e.g., Ba/La) as well as Ba/Th ratios with respect to leucite-free rocks.

Globally, the geochemistry of subduction-related volcanic rocks has been interpreted as reflecting the variable contribution of three main components affecting the mantle sources (e.g., Elliott, 2003): (1) a depleted mantle component (DM); (2) slab-derived fluids/supercritical liquids, with isotope compositions similar to that of subducted (and variably altered) basaltic oceanic crust (AOC); (3) slab-derived melts, with crust-like isotope signature, interpreted as deriving from the recycling of subducted sediments. *Fluid dominated* arcs (e.g., Tonga, Izu–Bonin, some Mariana islands; Elliott, 2003) show high Ba/Th > 1000 coupled with low $(La/Sm)_N$ values (around 1), as well as unradiogenic Sr isotope ratios. These features are consistent with experimental fluids/supercritical liquids generated during dehydration and partial melting of the subducted basaltic oceanic crust (Carter et al., 2015), which have been ascribed to the presence of residual epidote. On

Table 2
– Sr, Nd and Pb isotope composition of selected Ahar-Arasbaran igneous rocks. Both measured and initial values are reported. Sample characteristics and abbreviations as in Supplementary Table 2.

Sample	M-04	M-06	M-12	M-14	M-15	M-17	M-21	*M-25*	M-26	M-27	M-29
Lithology	Lava	Lava	Lava	Lava	Dike	Dike	Lava	*Lava*	Lava	Lava	Lava
Petrography	Lc-free	Lc-free	Lc-free	Lc-free			Lc-bearing	*Lc-bearing*	Lc-bearing	Lc-bearing	Lc-bearing
Rock-type	Tr-And.	Tr-And.	Tr-And.	Tr-And.	Trachite	Bas. Tr-And.	Tr-And.	*Tr-And.*	Tr-And.	Tr-And.	Tr-And.
Locality	Marallu	Marallu	Marallu	Marallu	Moradlu	Moradlu	Majid Abad	*Majid Abad*	Majid Abad	Majid Abad	Majid Abad
Age (Ma)	40.0	40.0	**40.0**	40.0	41.0	**41.0**	39.6	***39.6***	39.6	39.6	39.6
err	1.1	1.1	**1.1**	1.1	1.1	**1.1**	1.0	***1.0***	1.0	1.0	1.0
Rb (ppm)	71.8	71.3	55.2	88.1	156	41.3	103	*66***	119	37.0	144
Sr	1747	1547	913	1314	262	520	1802	*2018***	1914	1594	2152
$^{87}Sr/^{86}Sr$	0.704926	0.704920	0.704920	0.705089	0.706297	0.705836	0.704662	*0.704492*	0.704627	0.704560	0.704535
2se	0.000008	0.000007	0.000007	0.000006	0.000007	0.000007	0.000007	*0.000007*	0.000007	0.000007	0.000007
$(^{87}Sr/^{86}Sr)i$	0.704852	0.704840	0.704812	0.704959	0.705217	0.705669	0.704569	*0.704438*	0.704522	0.704513	0.704418
2se*	0.000010	0.000010	0.000011	0.000012	0.000082	0.000015	0.000010	*0.000008*	0.000010	0.000007	0.000011
Nd (ppm)	32.9	33.9	32.5	32.6	24.7	14.8	32.7	*nd*	24.6	33.5	30.2
Sm	6.17	6.49	6.15	6.22	4.28	3.33	5.94	*nd*	4.48	6.59	5.47
$^{143}Nd/^{144}Nd$	0.512643	0.512652	0.512653	0.512640	0.512655	0.512609	0.512754	*0.512737*	0.512747	0.512738	0.512738
2se	0.000005	0.000006	0.000005	0.000004	0.000005	0.000007	0.000005	*0.000005*	0.000005	0.000005	0.000006
$(^{143}Nd/^{144}Nd)i$	0.512614	0.512622	0.512623	0.512610	0.512627	0.512572	0.512725	*nc*	0.512718	0.512707	0.512709
2se*	0.000005	0.000007	0.000005	0.000004	0.000005	0.000007	0.000005	*nc*	0.000005	0.000005	0.000006
Pb** (ppm)	28	27	31	25	38	15	35	*29*	37	30	47
U	2.69	2.73	2.58	2.70	6.09	1.10	2.50	*nd*	1.86	2.01	3.04
Th	10.0	10.6	9.7	9.6	20.6	3.4	13.1	*9.2***	10.0	7.6	13.5
$^{206}Pb/^{204}Pb$	18.717	18.717	18.717	18.720	18.770	18.772	18.630	*18.633*	18.634	18.637	18.628
2se	0.002	0.002	0.003	0.002	0.002	0.003	0.002	*0.002*	0.002	0.002	0.003
$^{208}Pb/^{204}Pb$	38.844	38.842	38.861	38.838	38.893	38.896	38.735	*38.723*	38.747	38.738	38.707
2se	0.004	0.005	0.006	0.005	0.003	0.007	0.003	*0.005*	0.004	0.004	0.006
$^{207}Pb/^{204}Pb$	15.609	15.608	15.609	15.607	15.630	15.617	15.598	*15.596*	15.600	15.598	15.591
2se	0.002	0.002	0.003	0.002	0.001	0.003	0.001	*0.002*	0.002	0.002	0.003
$(^{206}Pb/^{204}Pb)i$	18.679	18.676	18.683	18.676	18.704	18.743	18.601	*nc*	18.613	18.611	18.602
2se*	0.011	0.012	0.010	0.012	0.014	0.011	0.010	*nc*	0.010	0.010	0.010
$(^{208}Pb/^{204}Pb)i$	15.608	15.606	15.607	15.605	15.627	15.616	15.596	*nc*	15.599	15.597	15.590
2se*	0.010	0.010	0.010	0.010	0.010	0.010	0.010	*nc*	0.010	0.010	0.010
$(^{207}Pb/^{204}Pb)i$	38.796	38.792	38.819	38.786	38.819	38.867	38.685	*nc*	38.712	38.705	38.669
2se*	0.032	0.031	0.032	0.030	0.033	0.031	0.031	*nc*	0.032	0.029	0.031

Inital values are calculated on the basis of the age of the different suites of rocks measured on selected representative samples (highlited in bold). Age propagated error (2se*) are obtained by Montecarlo simulation. Initial Nd and Pb values for samples in italic were not calculated (nc) since elemental abundances were not detecetd (nd).
*Cpx-rich.
**XRF data.

the contrary, *Sediment dominated* subduction related magmas are generally characterized by higher trace element content, radiogenic Sr, low Ba/Th and high La/Sm ratios (Elliott, 2003).

In this framework, leucite-bearing lavas share some geochemical similarities with the *fluid-dominated* arcs, being characterized by high Ba/Th (170–520) and relatively low $^{87}Sr/^{86}Sr_i$ (0.70439–0.70464) values, whereas leucite-free lavas mainly conform to *sediment dominated* ones, showing systematically lower Ba/Th (12–170) and higher $^{87}Sr/^{86}Sr_i$ (0.70481–0.70567) values (Fig. 11a). However, all the Arasbaran rocks (including leucite-bearing lavas) are characterized by high La/Sm ratios (2.7–5.7), incompatible with mantle sources affected only by AOC-derived fluids/supercritical liquids (Fig. 11b). In particular, leucite-bearing rocks plot outside the trend of global arc magmas (Fig. 11 data from Elliott, 2003), having too high La_N/Sm_N and Ba/Th with respect to typical *fluid dominated* and *sediment-dominated arcs*, respectively.

The unusual geochemical and isotopic composition of these magmas can be explained taking into account the experimental study of Skora et al. (2015) that tested the melting of undoped sediments, with variable amount of carbonate-component, at T-P conditions typical of subduction environments (3GPa and 800–1100 °C). They demonstrated that high-carbonate (HC) sediments can produce partial melts enriched in 'fluid-mobile' elements such Cs, Ba, Rb, K and Sr showing geochemical similarities with fluids conventionally ascribed to altered oceanic crust. On the other hand, HFSE such as Ti, Nb, and Ta are depleted, due to retention in residual rutile at temperature < 1000 °C, as well as Y, and HREE due to their compatibility in residual garnet or carbonate. These experiments also showed that the presence of residual epidote, during melting of HC sediment, resulted in melts with high Ba/Th, higher than those produced by carbonate-poor (LC) epidote-free lithologies. On the other hand, both LC and HC partial melts obtained at $T > 900$ °C produce high $(La/Sm)_N$ values (4.0–7.0) that may originate from the relative stabilities of epidote and garnet (Skora et al., 2015).

Accordingly, we suggest that both leucite-bearing and leucite-free magma types require a sedimentary input in their metasomatized mantle sources. Comparing our data with the experimental melts reported in Skora et al. (2015), the leucite-bearing rocks are consistent with the involvement of recycled carbonate-rich lithologies (HC), whilst carbonate-poor ones (LC) seem to prevail in the mantle source of leucite-free rocks.

Many of the geochemical features of leucite-bearing rocks are comparable to that of the Neapolitan district of the Roman volcanic province In Italy, for which a significant sedimentary (carbonate) contribution to the mantle source has been invoked (Conticelli and Peccerillo, 1992; Avanzinelli et al., 2009, 2018; Conticelli et al., 2015; Guarino et al., n.d. Fig. 11).

Sr-Nd-Pb isotopes provide further evidence that supports the involvement of sedimentary partial melts, rather than AOC fluids/

M-32	M-33	M-36	M-38	*M-39*	M-40	M-45	M-51	M-54	M-56	M-58	M-60
Pillow Lc-bearing Tr-And. Gheshlagh	Pillow Lc-bearing Tr-And. Gheshlagh	Columnar lava flow Lc-bearing Tr-And. Gheshlagh	Pillow Lc-bearing Tr-And. Gheshlagh	*Columnar lava flow Lc-bearing Tr-And. Gheshlagh*	Pillow Lc-bearing Bas.And.* Gheshlagh	Pillow Lc-bearing Tr-And. Gheshlagh	Lava Lc-bearing Tr-And. Moshiran	Lava Lc-free Bas. Tr-And. S.Moshiran	Lava Lc-free Bas. Tr-And. S.Moshiran	Lc-free Bas. Tr-And. Tulun	Lc-free Bas. Tr-And. Tulun
39.4	39.4	**39.4**	39.4	*39.4*	39.4	39.4	39.4	**41.9**	41.9	**41.1**	41.1
1.0	1.0	**1.0**	1.0	*1.0*	1.0	1.0	1.0	**1.1**	1.1	**1.1**	1.1
56.5	44.2	91.2	48.6	*30***	44.6	42.7	87.4	73.3	39.4	51.6	74.3
848	701	957	518	*1043***	2932	1594	1736	477	666	466	509
0.704574	0.704578	0.704684	0.704769	*0.704437*	0.704434	0.704681	0.704522	0.705305	0.705089	0.705173	0.705179
0.000007	0.000007	0.000008	0.000007	*0.000007*	0.000007	0.000006	0.000007	0.000007	0.000008	0.000007	0.000007
0.704479	0.704483	0.704521	0.704615	*0.704390*	0.704407	0.704640	0.704439	0.705045	0.704991	0.704977	0.704946
0.000010	0.000010	0.000015	0.000014	*0.000008*	0.000007	0.000007	0.000010	0.000020	0.000011	0.000016	0.000018
21.4	20.6	24.7	18.0	*nd*	17.1	18.6	27.1	26.7	21.9	20.8	25.5
4.15	4.02	4.69	3.54	*nd*	3.72	3.62	5.10	5.07	4.35	4.22	4.93
0.512818	0.512807	0.512804	0.512797	*0.512793*	0.512826	0.512782	0.512740	0.512642	0.512638	0.512640	0.512658
0.000008	0.000005	0.000007	0.000006	*0.000004*	0.000005	0.000006	0.000012	0.000006	0.000006	0.000006	0.000005
0.512787	0.512776	0.512774	0.512765	*nc*	0.512791	0.512751	0.512710	0.512611	0.512605	0.512607	0.512627
0.000008	0.000005	0.000007	0.000006	*nc*	0.000005	0.000006	0.000012	0.000006	0.000006	0.000006	0.000006
36	35	32	26	*33*	24	31	36	22	21	17	18
2.49	1.66	1.92	1.20	*nd*	1.32	2.02	3.18	3.56	1.43	1.54	2.81
6.8	6.8	7.3	6.0	*4.6***	4.8	7.8	12.1	14.9	5.8	6.1	11.4
18.667	18.621	18.669	18.599	*18.620*	18.628	18.637	18.664	18.707	18.670	18.717	18.739
0.002	0.002	0.003	0.001	*0.002*	0.003	0.002	0.003	0.001	0.002	0.002	0.002
38.691	38.691	38.710	38.663	*38.632*	38.742	38.744	38.749	38.868	38.780	38.835	38.857
0.005	0.003	0.007	0.002	*0.003*	0.006	0.004	0.007	0.003	0.004	0.004	0.005
15.574	15.576	15.573	15.571	*15.558*	15.584	15.596	15.597	15.643	15.622	15.626	15.627
0.002	0.001	0.003	0.001	*0.001*	0.002	0.002	0.003	0.001	0.001	0.002	0.002
18.639	18.602	18.645	18.581	*nc*	18.607	18.611	18.629	18.639	18.641	18.681	18.676
0.011	0.010	0.010	0.010	*nc*	0.010	0.011	0.011	0.013	0.010	0.011	0.014
15.573	15.575	15.572	15.570	*nc*	15.584	15.595	15.596	15.639	15.620	15.624	15.624
0.010	0.010	0.009	0.010	*nc*	0.010	0.010	0.010	0.010	0.010	0.010	0.010
38.666	38.666	38.680	38.633	*nc*	38.716	38.711	38.705	38.775	38.742	38.787	38.773
0.030	0.030	0.031	0.031	*nc*	0.030	0.032	0.031	0.034	0.030	0.031	0.032

supercritical liquids as a metasomatizing agents of the Arasbaran mantle section. Although the Sr isotopic composition of leucite-bearing rocks (among the least radiogenic values of the whole TIP) is compatible with those of the neighboring Neotethyan Mesozoic ophiolites (Fig. 9), representing the local subducted AOC, their low $^{143}Nd/^{144}Nd$ and high $^{207}Pb/^{204}Pb$ (Figs. 9, 10) clearly require the contribution of partial melts derived from sedimentary material.

In Figs. 9 and 10 we attempted to model a mixing between the possible end-members involved in the mantle source of the Ahar-Arasbaran igneous rocks, namely i) the pre-metasomatised mantle wedge, ii) the AOC derived fluids/supercritical liquids and iii) the two types of sediments partial melts. The proposed model is clearly a simplification of a much more complex process. In fact, there are several parameters which are difficult to constrain, including the precise compositions of the end-members and the metasomatic reactions in the mantle. Since the pioneering studies of Foley (1992), several studies have argued that such an interaction produces phlogopite/amphibole-rich metasomatic veins or domains whose mineralogy depends on the nature of the sediment melts (e.g., Avanzinelli et al., 2020; Conticelli et al., 2015; Dai et al., 2014; Gülmez et al., 2023). Silica-rich sedimentary melts would stabilize orthopyroxene at the expenses of olivine (Avanzinelli et al., 2020; Conticelli et al., 2015), whilst carbonate-rich ones would produces wherlitic metasomes enriched in olivine and clinopyroxene (Conticelli et al., 2015; Gülmez et al., 2023). In addition, the isotopic composition of these metasomatic domains may be heterogeneous, as recently demonstrated by Avanzinelli et al. (2020).

Hereafter, we attempt to model this complex process considering the possible endmembers involved in the genesis of the Arasbaran magmas, in order to reproduce the geochemical and isotopic composition of the studied igneous rocks.

The composition of the pre-metasomatised mantle wedge and of AOC have been estimated considering the least metasomatised/altered mantle rocks and mafic rocks from Neyriz (Shafaii Moghadam et al., 2014) and Kermanshash (Saccani et al., 2013) ophiolites, respectively, since they represent remnants of the Neotethyan mantle and oceanic crust involved in this subduction system. Carbonate-rich (HC) and carbonate-poor (LC) marly sediments melts (see details below) were instead used as "proxy" for the composition of sedimentary metasomatic agents (e.g., Avanzinelli et al., 2018). The least differentiated volcanics ($Mg\# > 0.60$, $SiO_2 < 55$ wt%) from the leucite-bearing (samples M36, M38; M45) and the leucite-free (M54, M56, M58, M60) groups were chosen as the target compositions of the genetic model since they reasonably represent the most suitable parental magma types of the area. The results of elemental and isotopic based mass balance calculations, together with those of the non-modal melting model, highlight that both fluids/supercritical liquids and sediment melts need to be added to the mantle wedge to reproduce the source of leucite-bearing and leucite-free magmas of the Arasbaran area.

In particular, we infer that the geochemical signature of the mantle source is achieved through a two-steps process, a first enrichment event due to the addition of AOC-derived fluids/supercritical liquids to the local mantle wedge, followed by a second one involving different proportions and lithologies of sedimentary components.

In our model, the addition of 5–6% of AOC component (represented by the average Zagros MORB ophiolites) to the pre-subduction local mantle wedge can be inferred as a ubiquitous enrichment stage that characterized the whole mantle section source (S1) of the Arasbaran magmas. The composition of the slab derived fluids/supercritical liquids

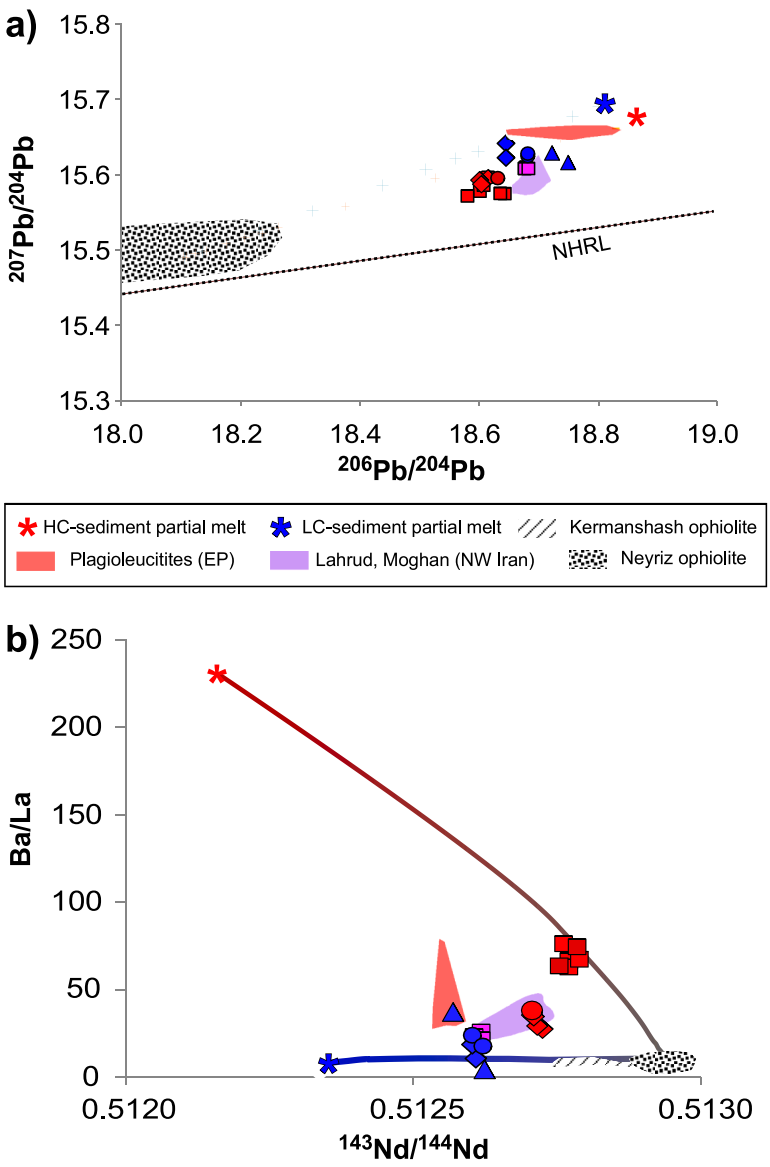

Fig. 10. – a) Initial Pb isotope ratios ($^{207}Pb/^{204}Pb$ vs $^{206}Pb/^{204}Pb$) and b) Ba/La vs $^{143}Nd/^{144}Nd$ of leucite-bearing and leucite-free igneous rocks from the Ahar-Arasbaran region (NW Iran). The distribution of nearly coeval leucite-bearing and leucite-free rocks from NW Iran (Lahrud – Shafaii Moghadam et al., 2018; Moghan – Amraee et al., 2019) and from Eastern Pontides (Altherr et al., 2008; Eyuboglu et al., 2011) are also reported for comparison. Red and blue solid lines represent the mixing trends between the average of subducted oceanic crust, represented by Neyriz (Shafaii Moghadam et al., 2014) and Kermanshash (Saccani et al., 2013) Neotethyan ophiolites (Ba/La = 5–10, $^{143}Nd/^{144}Nd$ = 0.51277–0.51299), a high-carbonate (HC) sediment (Apennine marl SD48 – Avanzinelli et al., 2018; Ba/La = 230, $^{143}Nd/^{144}Nd$ = 0.512163) and a low-carbonate sediment (average Mariana pelagic clays 800 and 801- Plank and Langmuir, 1998; Ba/La = 4.6, $^{143}Nd/^{144}Nd$ = 0.512135) partial melts. Bulk/melt ratios are taken from the experimental work of Skora et al. (2015) for HC and LC sediments at temperatures of 850–900 °C. The Northern Hemisphere Reference Line (NHRL) is from Hart (1984). Symbols as in Fig. 4.

was obtained by the application of experimental results of (Carter et al., 2015) at 3 GPa and temperature between 900 and 1000 °C to the average local MORB-type ophiolites. The second enrichment stage, was instead distinct in terms of nature and proportions of the sedimentary component, differentiating the mantle sources of the leucite-bearing (S2) and leucite-free (S3) magma types. In particular, the addition of a small amount (3–4%) of a HC-dominated (80–90%) sediment partial melts to the enriched mantle wedge successfully reproduces the isotopic composition of the most undersaturated leucite-bearing lavas, whereas higher proportions (4–8%) of LC-dominated (60–80%) sediment melts are needed to reproduce the isotopic features of the less undersaturated leucite-free lavas (Fig. 9). The two distinct isotopic trends defined by the second enrichment stage (Fig. 9) originated from the different isotopic and elemental budget of the HC and LC sediment partial melts, which are characterized by a Sr/Nd ratio higher (Sr/Nd > 100) and lower (Sr/Nd < 20), respectively, with respect to the S1 source (Sr/Nd ca. 70). The composition of the sediment partial melts was obtained by the application of the experimental results of (Skora et al., 2015) performed at 3 GPa pressure and 900–1000 °C temperature to the HC and LC Mediterranean marly sediments reported in Avanzinelli et al. (2018) and Plank and Langmuir (1998), respectively.

The calculated geochemical compositions of the mantle sources were used as input for the magma genesis melting model to reproduce the observed incompatible elements distribution of the leucite-bearing and leucite-free magmas (Fig. 12). The best fit for the leucite-bearing magma-type is obtained by low melting degree (F around 4%) of the

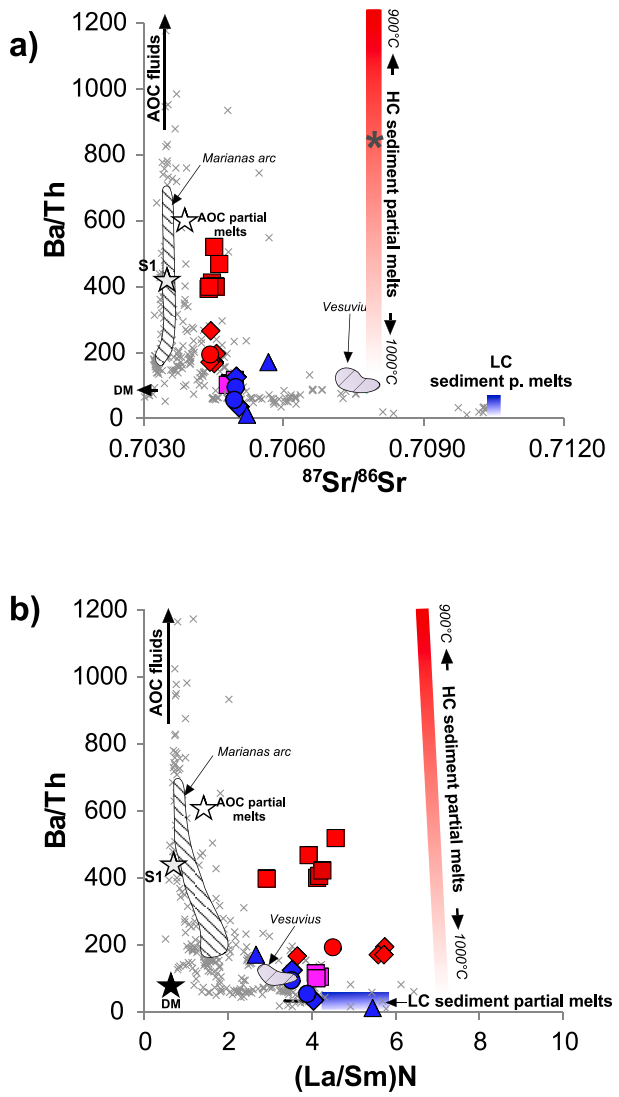

Fig. 11. – Ba/Th vs. $^{87}Sr/^{86}Sr_{(i)}$ (a) and vs. $(La/Sm)_N$ (b) showing the distribution of leucite-bearing and -free lavas from the Ahar-Arasbaran region. The composition of worldwide arc magmas, as well as the fields of Mariana arc (representative of AOC predominant fluid metasomatism) and of Neapolitan district of the Roman province (Vesuvius, representative of predominant carbonate melt metasomatism) are shown for comparison. Data from Elliott et al. (1997) and Avanzinelli et al. (2018).

S2 mantle source (Ol_{54}, Opx_{25}, Cpx_{12}, Sp_2, Gt_3, $Amph_2$, Phl_1), whereas a higher melting degree (F around 10%) of the S3 source (Ol_{54}, Opx_{25}, Cpx_9, Sp_3, Gt_3, $Amph_2$, Phl_4) is required to fit the distribution of the leucite-free magmas (Fig. 12). The difference in the composition and partial melting degree of these two mantle sources is corroborated by the incompatible element distribution of leucite-free magmas, which is very similar to that of the LC-dominated sedimentary component. In this model, the composition of the High-Carbonate and Low-Carbonate sediment partial melts at temperatures between 900 and 1000 °C were tested as the sedimentary metasomatic agents, since they are the main carrier of REE (especially LREE). The results of our genetic model clearly indicate that, although AOC fluids/supercritical liquids can imprint some geochemical features typical of Arasbaran magmas (high K, Sr, Ba/Th), they cannot provide the proper LREE budget to the mantle sources. As indicated by recent studies (e.g., Rustioni et al., 2021) REE mobilization from the oceanic slab could be achieved also through the interaction with saline fluids. However, the application of these experimental results to the genetic model of Arasbaran magma fails to reproduce some geochemical features, such as Ba/Th and Th/LREE ratios. Moreover, as reported in Li et al. (2022), the addition of 2–3% of such saline fluids to the mantle source would produce a high H_2O content (>10 wt%) magma, which is inconsistent with the absence of hydrous phases in leucite-bearing lavas. Therefore, the addition of the AOC component alone to the depleted mantle wedge cannot explain the observed isotopic features of the Arasbaran lavas, which need a metasomatically overprinted source by a sedimentary component.

The different incompatible element budget provided by the two sedimentary components is reflected by the distinct geochemical composition of the S2 and S3 modelled mantle source. The S2 source is generally less enriched than S3 source and this is consistent with their modal metasomatism. S2 is characterized by a lower content of hydrous accessory phases (phlogopite+amphibole = 3) than S3 (phlogopite+amphibole = 6), but more enriched in clinopyroxene as expected for the interaction between carbonate-rich melts and peridotitic mantle (Conticelli et al., 2015; Gülmez et al., 2023). S2 also displays distinctly higher Ba/Th, Sr/Nd and Sr/Y with respect to S3 source, consistent with the geochemical features observed in the leucite-bearing and leucite-free lavas, respectively. In fact, the distinct melting degrees of S2 and S3 required to generate the related magma-types further emphasize these geochemical differences in the modelled melts (in particular for the Ba/Th and Sr/Y).

The isotopic composition of the Arasbaran ultrapotassic magmas is characterized by the least radiogenic Sr and most radiogenic Nd values of the area (Lahrud: Shafaii Moghadam et al., 2018; Salavat Range: Soltanmohammadi et al., 2021; Moghan: Amraee et al., 2019). At a regional scale, analogies and differences can be highlighted between the subduction-related igneous rocks of NW Iran and Central-Eastern Pontides sectors of the Alpine-Himalayan belt. The similarity is represented by the less radiogenic values showed by ultrapotassic leucite-bearing rocks with respect to shoshonitic leucite-free rocks in both sectors. The difference is a general displacement toward more radiogenic values of both rock types in the Eastern Pontides sector with respect to NW Iran. This is in excellent agreement with the general isotopic trend of the Cenozoic ultrapotassic (lamproitic) magmatism along the Alpine-Himalayan belt identified by Casalini et al. (2022), probably indicating that similar sedimentary end-members (i.e., HC and LC sediments) are involved, but at decreasing proportion from W to E with respect the to the ambient mantle. Using the same components, the Pb isotope systematics also allows to reproduce leucite-bearing rocks as a mixing between the inferred subducted oceanic crust and HC-sediment partial melts and leucite-free rocks with Low-Carbonate sediment partial melts, the latter showing comparatively more radiogenic Pb values (Fig. 10a). Coherently, the Pb isotopic values confirm that the metasomatic agents of the leucite-bearing rocks are characterized by a lower sediment contribution with respect to those of leucite-free rocks.

Similar results can be obtained using elemental ratios such as Ba/La and Nd isotopic composition, confirming the reliability of the model and the source heterogeneity that characterizes the mantle section of the Arasbaran area (Fig. 10b). Other geochemical features of leucite-bearing rocks, such as the high Sr/Y (up to 300) and Eu/Eu* (1.05–1.15) are compatible with the involvement of marine carbonate sediment as metasomatic component of their mantle source (Nagarajan et al., 2011).

5.3. *Evolution of the Arasbaran mantle sources*

Geochronological K—Ar data indicate a nearly coeval generation of the Arasbaran leucite-bearing (39.4–39.6 +/− 1.0 Ma) and -free (41.9 +/− 1.1 Ma) magmatism in the Middle-Late Eocene, in agreement with previous data on hypabyssal rocks from the same area (42.7–38.4 Ma, Alberti et al., 1980). The significant variability of the magmatic products occurred over a limited area in this short time-span indicate that this event represents an important step in the magmatic evolution of the Ahar-Arasbaran region. This is also confirmed by the intermediate age (40.0 +/− 1.1 Ma) showed by the *Marallu* rocks, which show

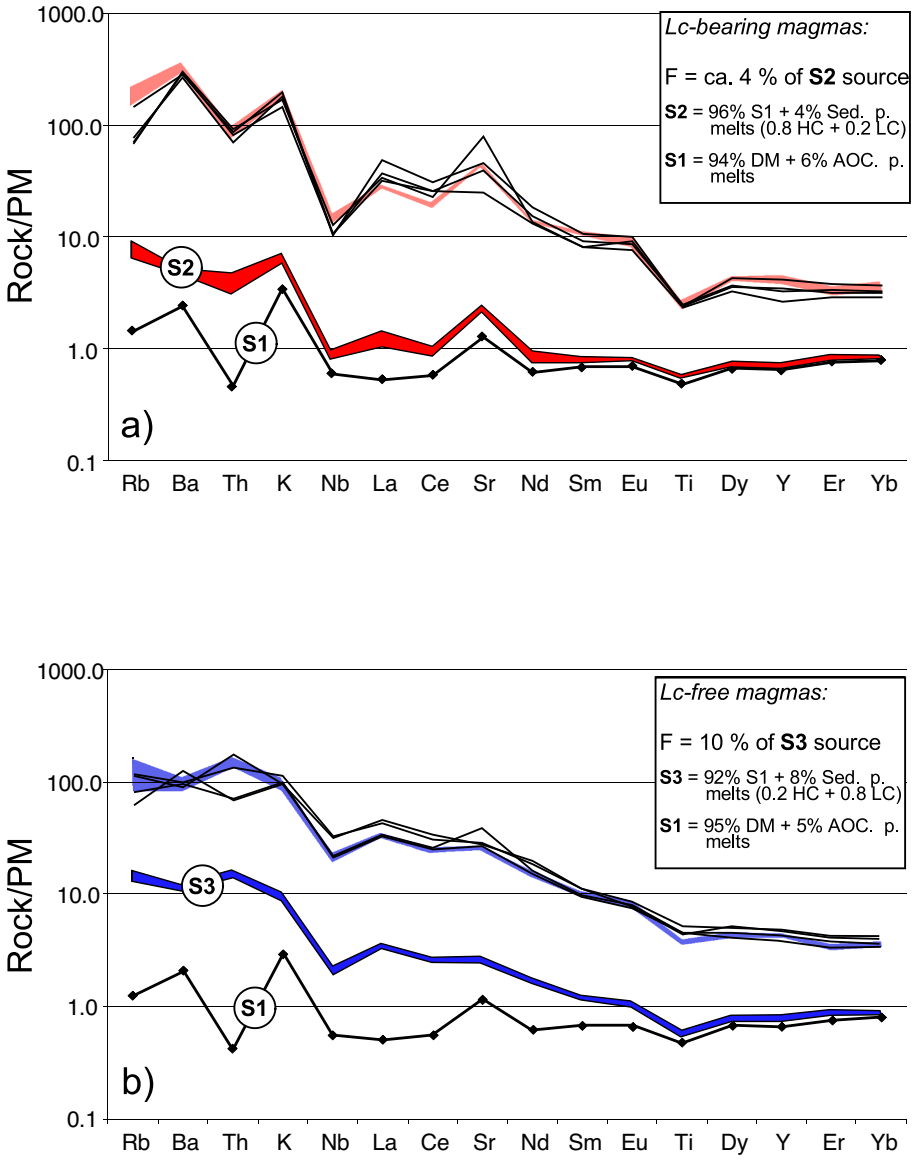

Fig. 12. – Non-modal partial melting model for the leucite-bearing (a) and -free (b) Arasbaran magmas. The red field represents the compositional variation of magmas produced by S2 and S3 mantle sources metasomatised by sediment partial melts produced at 900–1000 °C (Skora et al., 2015). Partition coefficient from the GERM database (https://kdd.earthref.org/KdD) and from La Tourette et al. (1995). End-member lithologies and compositions as in Fig. 9. See text for further details. (For interpretation of the references to colour in this figure legend, the reader is referred to the web version of this article.)

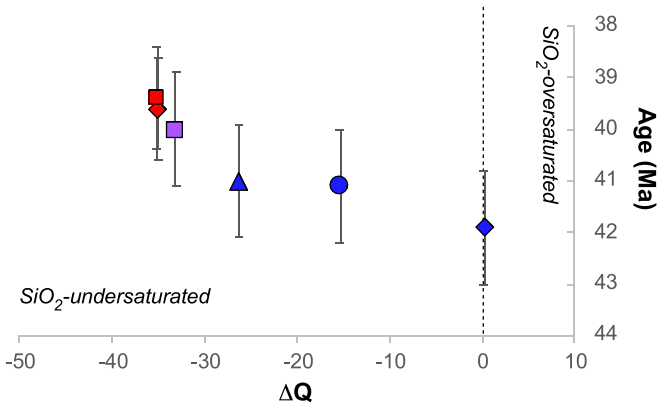

Fig. 13. – Δq vs age (Ma) distribution of leucite-bearing and leucite-free igneous rocks from the Ahar-Arasbaran region (NW Iran). Age analytical errors (Table 2) are expressed by error bars.

petrographic, geochemical and isotopic evidence of mixing between older leucite-free and younger leucite-bearing rocks, with the former predominating over the latter. The spatio-temporal relationships of these different magmatic episodes suggest that during Middle Eocene magmatism in the Arasbaran area slightly migrated northwestward, becoming progressively more silica-undersaturated (Fig. 13). A similar temporal transition from silica-saturated to -undersaturated products is observed in the ultrapotassic rocks from Italy (Avanzinelli et al., 2009; Conticelli et al., 2015). The elemental and isotopic features of peri-Tyrrhenian ultrapotassic rocks require the involvement of a significant proportion of sedimentary melt component in their mantle source (Avanzinelli et al., 2009; Conticelli et al., 2009), able to create net veined metasomatic domains. Italian peri-Tyrrhenian magmatism displays a further clear temporal succession from ultrapotassic, to shoshonitic and high-K calc-alkaline magmatism: This transition was interpreted as due to the progressive involvement of host mantle rocks over the metasomatic veins at increasing mantle melting degrees, in response to isotherm relaxation following the Neotethyan slab roll-back in the mature subduction geodynamics (Avanzinelli et al., 2009; Bianchini et al., 2008; Conticelli et al., 2009, 2015).

The Arasbaran magmas display an opposite transition from shoshonitic leucite-free to ultrapotassic leucite bearing magmas, but their geochemical and isotopic composition also require a significantly lower contribution of the sedimentary component, arguing against the creation of a net veined mantle source, but rather a more diffused metasomatism of the peridotitic mantle wedge.

This sector of the Alpine-Himalayan belt, is characterized since the Cretaceous onward, by a northeastward subduction of the Neotethys oceanic slab underneath the southern margin of the Eurasia plate, followed by continental collision starting from the Oligocene in northwestern Iran with a progressive SW migration of deformation and topography (Agard et al., 2011; Aghazadeh et al., 2011). In this geodynamic scenario, the Middle Eocene Ahar-Arasbaran magmatism could represent a subduction-related event, triggered by slab retreat and roll-back (Fig. 14; Rabiee et al., 2019 and references therein). The slab roll-back and retreat caused lithospheric extension in NW Iran (Shafaii Moghadam et al., 2018 and references therein) leading to asthenospheric up-welling that caused heating and lithosphere erosion through the melting of the metasomatised mantle wedge, the so called "magmatic flare-up" that was particularly intense during Eocene (Verdel et al., 2011). In this framework, the melting of leucite-free (S3) and bearing (S2) sources occurred slightly diachronous and zonally arranged (Fig. 14a) probably both for the late arrival of high carbonate sediments at depth in concomitance with incipient slab steepening and roll back (e.g., Conticelli et al., 2015). The higher melting degree of S3 with respect to S2 source predicted by the model can be explained by the isotherms geometry in the mantle wedge generated in response to the slab retreat geodynamic trigger (e.g., Frezzotti et al., 2009) as well as by the higher proportion of metasomatic lower solidus component in the mantle source. In this scenario an eastward dipping polarity of the subduction plane broadly fits with the observed distribution in space and time of the associated magmatism, with the S2 source located relatively closer to the subducted slab with respect to the S3 source (Fig. 14b).

The Eocene Ahar-Arasbaran melting sequence from shoshonitic to ultrapotassic parallels the time-dependent geochemical variation observed from Late Cretaceous in Central Anatolia (Gülmez et al., 2016) through Paleocene in the eastern Pontides (Eyuboglu et al., 2011).

The Ahar-Arasbaran leucite-bearing rocks are very similar to plagioleucicites, a rare volcanic product worldwide, that at a regional scale can be compared with some Paleocene occurrences from Eastern Everek Hanları (Altherr et al., 2008) and Southern Pontides (Ankara: Çapan, 1984). These magmatic products are more common in other sectors of the Alpine-Himalayan belt, such as the Roman volcanic province in central-southern Italy (Avanzinelli et al., 2009; Conticelli et al., 2015), which however display significantly more enriched compositons (see above). In particular, the Arasbaran rocks show intermediate geochemical composition between the Paleocene Anatolian plagioleucitites and those from the Neapolitan district of the Roman magmatic province (Supplementary Fig. 3). The generation of the Neapolitan plagioleucitites was interpreted as the result of partial melting of previously metasomatized mantle further enriched by the addition of carbonate sediments melts (Avanzinelli et al., 2018). A similar genetic model is proposed for the Arasbaran leucite-bearing rocks, but with a different metasomatic agent characterized by a lower sediment/altered oceanic crust ratio. This is consistent with the observed differences in the isotopic and trace element composition of the NW Iran, Anatolian and Italian plagioleucitites (Fig. 10).

6. Conclusions

The Middle Eocene K-rich magmatism of the Ahar-Arasbaran region in NW Iran vary from shoshonitic to ultrapotassic affinity, the latter representing a relatively rare occurrence in this sector of the Alpine-Himalayan belt. This magmatic event is related to the melting of mantle sources variously metasomatised by different sedimentary and mafic components during the Neotethys subduction under the Eurasian plate, triggered by slab roll-back and tearing after the Late Cretaceous-Early Eocene Arabian-Eurasian continental collision. The geochemical features of ultrapotassic leucite-bearing magmas are compatible with the involvement of a limited contribution (4–5%) of HC-sediment melts to a mantle source previously metasomatized by AOC-derived fluids/supercritical liquids. On the other hand, a higher (7–8%) LC-sedimentary partial melt component (added to a similar AOC-modified mantle wedge) is required to generate the shoshonitic leucite-free magmas. The almost coeval eruption of both magma types indicates a common geodynamic trigger, which produced earlier a relatively high-melting degree event of the S3 source, to generate the leucite-free shoshonites, and later low degree melts of the S2 source, to generate the leucite-bearing ultrapotassic rocks. The latter occurred at lower temperature being closer to the subducted slab and characterized by a lesser amount of a lower solidus domains. The relative distance from the slab of the two metasomatic domains is probably due to the late arrival of HC- with respect to LC-sediment to the trench due to the evolution of the subduction system toward the continental collision. This would have produced the observed distribution of the Ahar-Arasbaran lavas, with the ultrapotassic magmas mainly located to the NW and shoshonitic magmas in the SE part of the area. The similarities in the nature of the metasomatic agents and in the geodynamic evolution with the Mediterranean subduction-related magmatism suggest commonalities along the whole Alpine-Himalayan belt, whereas the distinctly lower sedimentary contribution to the mantle sources of the Ahar-Arasbaran magmas confirm the decreasing W-E trend observed along these

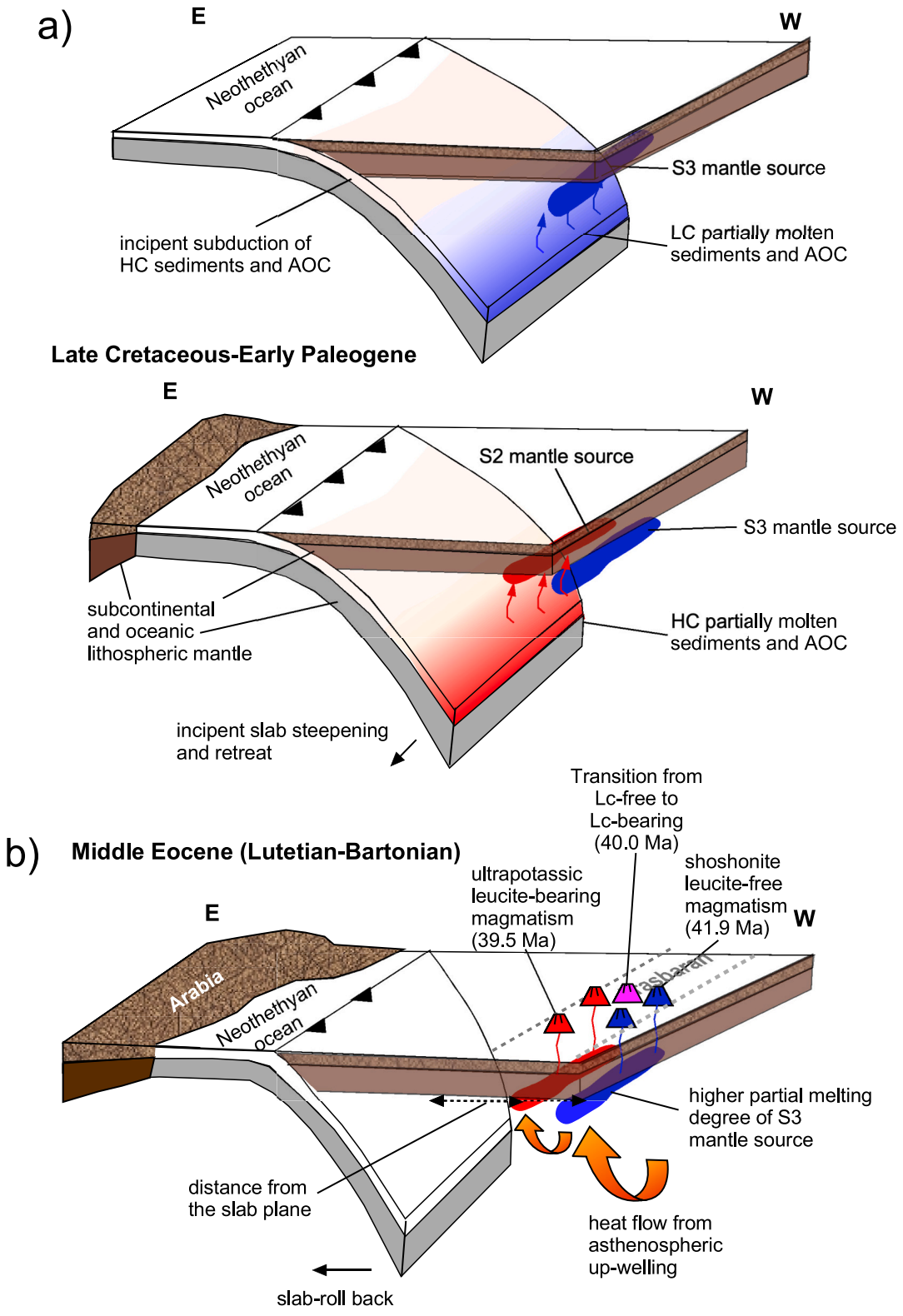

Fig. 14. – Geodynamic sketch depicting the generation of the leucite-bearing and leucite-free magmas in the Arasbaran area (Ardabil Province, NW Iran). During late Cretaceous the subducting Neotethyan plate brought first at the depth of melting (around 3 GPa, Shafaii Moghadam et al., 2018) LC-sediment (a), which were followed by the late arrival of HC-sediments at similar melting conditions (e.g., Skora et al., 2015) due to slab verticalization and retreat at a more mature stage of subduction (e.g., Conticelli et al., 2015), with the creation of two distinct metasomatic domains (S3 and S2) in the mantle wedge (b). In the Eocene, slab roll-back and retreat recalling asthenospheric up-welling and heat flow to the overlying mantle wedge. Melting of the mantle metasomatised domains that produced the Arasbaran volcanism started from and was more effective on mantle domains at a higher distance from the colder subducting plate, i.e., from the S3 source, progressively involving sectors of mantle wedge located closer to the Neotethyan slab that suffered a lower thermal perturbation (c).

subduction systems.

Supplementary data to this article can be found online at https://doi.org/10.1016/j.lithos.2024.107504.

Declaration of competing interest

The authors declare that they have no known competing financial interests or personal relationships that could have appeared to influence the work reported in this paper.

Acknowledgements

We thank Renzo Tassinari and Paolo Di Giuseppe for lab assistance. This study was supported by the Iran National Science Foundation (INSF) grant # 4012817 issued to Mehraj Aghazadeh, the Payam-e-Noor University, MUR funding through PRIN grants 20158A9CBM and 2015EC9PJ5 issued to S. Conticelli and R. Avanzinelli, respectively, and ex-60% grants of the University of Florence issued to C. Natali and M. Casalini.

References

Agard, P., Omrani, J., Jolivet, L., Whitechurch, H., Vrielynck, B., Spakman, W., Monie, P., Meyer, B., Wortel, R., 2011. Zagros orogeny: a subduction-dominated process. Geol. Mag. 148, 692–725. https://doi.org/10.1017/S001675681100046X.

Aghazadeh, M., Castro, A., Omran, N.R., Emami, M.H., Moinvaziri, H., Badrzadeh, Z., 2010. The gabbro (shoshonitic)–monzonite–granodiorite association of Khankandi pluton, Alborz Mountains, NW Iran. J. Asian Earth Sci. 38, 199–219. https://doi.org/10.1016/j.jseaes.2010.01.002.

Aghazadeh, M., Castro, A., Badrzadeh, Z., Vogt, K., 2011. Post-collisional polycyclic plutonism from the Zagros hinterland: the Shaivar Dagh plutonic complex, Alborz belt, Iran. Geol. Mag. 148, 980–1008. https://doi.org/10.1017/S0016756811000380.

Agostini, S., Di Giuseppe, P., Manetti, P., Savaşçın, M.Y., Conticelli, S., 2022. Geochemical and isotopic (Sr-Nd-Pb) signature of crustal contamination in Na-alkali basaltic magmas of South-East Turkey. Ital. J. Geosci. 141, 363–384. https://doi.org/10.3301/IJG.2022.21.

Akal, C., 2008. K-richterite-olivine-phlogopite-diopside-sanidine lamproites from the Afyon Volcanic Province, Turkey. Geol. Mag. 145, 570–575. https://doi.org/10.1017/S0016756808004536.

Alberti, A.A., Comin-Chiaramonti, P., Sinigoi, S., Nicoletti, M., Petrucciani, C., 1980. Neogene and quaternary volcanism in Eastern Azerbaijan (Iran): some K-Ar age determinations and geodynamic implications. Geol. Rundsch. 69, 216–225. https://doi.org/10.1007/BF01869034.

Allen, M., Armstrong, H., 2008. Arabia–Eurasia collision and the forcing of mid-Cenozoic global cooling. Palaeogeogr. Palaeoclimatol. Palaeoecol. 265, 52–58. https://doi.org/10.1016/j.palaeo.2008.04.021.

Altherr, R., Topuz, G., Siebel, W., Şen, C., Meyer, H.-P., Satır, M., Lahaye, Y., 2008. Geochemical and Sr–Nd–Pb isotopic characteristics of Paleocene plagioleucitites from the Eastern Pontides (NE Turkey). Lithos 105, 149–161. https://doi.org/10.1016/j.lithos.2008.03.001.

Amraee, A., Zareisahamieh, R., Moayyed, M., Ahmadikhalaji, A., Azimzadeh, A., Santos, J.F., 2019. Peshtasar basalts: an example of post-collision basalts in sedimentary basin of Moghan, NW Iran. J. Earth Syst. Sci. 128, 1–22. https://doi.org/10.1007/s12040-019-1083-z.

Avanzinelli, R., Lustrino, M., Mattei, M., Melluso, L., Conticelli, S., 2009. Potassic and ultrapotassic magmatism in the circum-Tyrrhenian region: significance of carbonated pelitic vs. pelitic sediment recycling at destructive plate margins. Lithos 113, 213–227. https://doi.org/10.1016/j.lithos.2009.03.029.

Avanzinelli, R., Casalini, M., Elliott, T., Conticelli, S., 2018. Carbon fluxes from subducted carbonates revealed by uranium excess at Mount Vesuvius, Italy. Geology 46, 259–262. https://doi.org/10.1130/G39766.1.

Avanzinelli, R., Bianchini, G., Tiepolo, M., Jasim, A., Natali, C., Braschi, E., Dallai, L., Beccaluva, L., Conticelli, S., 2020. Subduction-related hybridization of the lithospheric mantle revealed by trace element and Sr-Nd-Pb isotopic data in composite xenoliths from Tallante (Betic Cordillera, Spain). Lithos 352–353, 105316. https://doi.org/10.1016/j.lithos.2019.105316.

Beccaluva, L., Bianchini, G., Mameli, P., Natali, C., 2013. Miocene shoshonite volcanism in Sardinia: Implications for magma sources and geodynamic evolution of the Central-Western Mediterranean. Lithos 180–181. https://doi.org/10.1016/j.lithos.2013.08.006.

Bianchini, G., Beccaluva, L., Siena, F., 2008. Post-collisional and intraplate Cenozoic volcanism in the rifted Apennines/Adriatic domain. Lithos 101, 125–140. https://doi.org/10.1016/j.lithos.2007.07.011.

Bianchini, G., Braga, R., Langone, A., Natali, C., Tiepolo, M., 2015. Metasedimentary and igneous xenoliths from Tallante (Betic Cordillera, Spain): Inferences on crust-mantle interactions and clues for post-collisional volcanism magma sources. Lithos 220–223, 191–199. https://doi.org/10.1016/j.lithos.2015.02.011.

Boari, E., Avanzinelli, R., Melluso, L., Giordano, G., Mattei, M., De Benedetti, A., Morra, V., Conticelli, S., 2009. Isotope geochemistry (Sr–Nd–Pb) and petrogenesis of leucite-bearing volcanic rocks from "Colli Albani" volcano, Roman Magmatic Province, Central Italy: inferences on volcano evolution and magma genesis. Bull. Volcanol. 71, 977–1005. https://doi.org/10.1007/s00445-009-0278-6.

Bohrson, W.A., Spera, F.J., Heinonen, J.S., Brown, G., Scruggs, M., Adams, J., Takach, M., Zeff, G., Suikkanen, E., 2020. Diagnosing open-system magmatic processes using the Magma Chamber Simulator (MCS): part I—major elements and phase equilibria. Contrib. Mineral. Petrol. 175, 104. https://doi.org/10.1007/s00410-020-01722-z.

Bragagni, A., Mastroianni, F., Münker, C., Conticelli, S., Avanzinelli, R., 2022. A carbon-rich lithospheric mantle as a source for the large CO2 emissions of Etna volcano (Italy). Geology 50, 486–490. https://doi.org/10.1130/G49510.1.

Çapan, U.Z., 1984. Ankara melanjı içindeki zeolitli alkali bazaltik volkanizmanın karakteri ve yaşı hakkında. Türkiye Jeoloji Kurumu 38. Bilimsel ve Teknik Kurultayı, Bildiri özetleri, pp. 121–123.

Carter, L., Skora, S., Blundy, J., De Hoog, J., Elliott, T., 2015. An Experimental Study of Trace Element Fluxes from Subducted Oceanic Crust. J. Petrol. 56, 1585–1606. https://doi.org/10.1093/petrology/egv046.

Casalini, M., Avanzinelli, R., Tommasini, S., Natali, C., Bianchini, G., Prelević, D., Mattei, M., Conticelli, S., 2022. Petrogenesis of Mediterranean lamproites and associated rocks: the role of overprinted metasomatic events in the post-collisional lithospheric upper mantle. Geol. Soc. London Spec. Publ 513, 271–296. https://doi.org/10.1144/SP513-2021-36.

Castro, A., Aghazadeh, M., Badrzadeh, Z., Chichorro, M., 2013. Late Eocene-Oligocene post-collisional monzonitic intrusions from the Alborz magmatic belt, NW Iran. An example of monzonite magma generation from a metasomatized mantle source. Lithos 180–181, 109–127. https://doi.org/10.1016/j.lithos.2013.08.003.

Çoban, H., Flower, M., 2007. Late Pliocene lamproites from Bucak, Isparta (southwestern Turkey): Implications for mantle 'wedge' evolution during Africa-Anatolian plate convergence. J. Asian Earth Sci. 29, 160–176. https://doi.org/10.1016/j.jseaes.2006.06.006.

Comin-Chiaramonti, P., Meriani, S., Mosca, R., Sinigoi, S., 1979. On the occurrence of analcime in the northeastern Azerbaijan volcanics (northwestern Iran). Lithos 12, 187–198. https://doi.org/10.1016/0024-4937(79)90003-3.

Comin-Chiaramonti, P., Ruberti, E., Cundari, A., De Min, A., Gittins, J., Gomes, C., Gwalani, l, 2009. Genesis of Analcime and Nepheline-Potassium Feldspar-Kalsilite Intergrowths : a Review. Acta Vulcanol. 21, 123–132.

Conticelli, S., Peccerillo, A., 1992. Potassic and ultrapotassic volcanism from Central Italy: compositional characteristics, petrogenesis and inferences on the evolution of the mantle source. Lithos 28, 221–240. https://doi.org/10.1016/0024-4937(92)90008-M.

Conticelli, S., Francalanci, L., Manetti, P., Cioni, R., Sbrana, A., 1997. Petrology and geochemistry of the ultrapotassic rocks from the Sabatini Volcanic District, Central Italy: the role of evolutionary processes in the genesis of variably enriched alkaline magmas. J. Volcanol. Geotherm. Res. 75, 107–136. https://doi.org/10.1016/S0377-0273(96)00062-5.

Conticelli, S., Guarnieri, L., Farinelli, A., Mattei, M., Avanzinelli, R., Bianchini, G., Boari, E., Tommasini, S., Tiepolo, M., Prelević, D., Venturelli, G., 2009. Trace elements and Sr–Nd–Pb isotopes of K-rich, shoshonitic, and calc-alkaline magmatism of the Western Mediterranean Region: Genesis of ultrapotassic to calc-alkaline magmatic associations in a post-collisional geodynamic setting. Lithos 107, 68–92. https://doi.org/10.1016/j.lithos.2008.07.016.

Conticelli, S., Avanzinelli, R., Marchionni, S., Tommasini, S., Melluso, L., 2011. Sr-Nd-Pb isotopes from the Radicofani Volcano, Central Italy: constraints on heterogeneities in a veined mantle responsible for the shift from ultrapotassic shoshonite to basaltic andesite magmas in a post-collisional setting. Mineralogy and Petrology (Springer-Verlag, Heidelberg, Germany) 103, 123–148. https://doi.org/10.1007/s00710-011-0161-y available online 29 July 2011.

Conticelli, S., Avanzinelli, R., Ammannati, E., Casalini, M., 2015. The role of carbon from recycled sediments in the origin of ultrapotassic igneous rocks in the Central Mediterranean. Lithos 232, 174–196. https://doi.org/10.1016/j.lithos.2015.07.002.

Dai, L.-Q., Zhao, Z.-F., Zheng, Y.-F., 2014. Geochemical insights into the role of metasomatic hornblendite in generating alkali basalts. Geochem. Geophys. Geosyst. 15, 3762–3779. https://doi.org/10.1002/2014GC005486.

Dallai, L., Bianchini, G., Avanzinelli, R., Natali, C., Conticelli, S., 2019. Heavy oxygen recycled into the lithospheric mantle. Sci. Rep. 9, 8793. https://doi.org/10.1038/s41598-019-45031-3.

Dallai, L., Bianchini, G., Avanzinelli, R., Deloule, E., Natali, C., Gaeta, M., Cavallo, A., Conticelli, S., 2022. Quartz-bearing rhyolitic melts in the Earth's mantle. Nat. Commun. 13, 7765. https://doi.org/10.1038/s41467-022-35382-3.

Dilek, Y., Imamverdiyev, N., Altunkaynak, Ş., 2010. Geochemistry and tectonics of Cenozoic volcanism in the Lesser Caucasus (Azerbaijan) and the peri-Arabian region: collision-induced mantle dynamics and its magmatic fingerprint. Int. Geol. Rev. 52, 536–578. https://doi.org/10.1080/00206810903360422.

Doglioni, C., Agostini, A., Crespi, M., Innocenti, F., Manetti, P., Riguzzi, F., Savasci, Y., 2002. On the extension in western Anatolia and the Aegean Sea. J. Virtual Explor. 8 https://doi.org/10.3809/jvirtex.2002.00049.

Elliott, T., 2003. Tracers of the Slab. Geophys. Monogr. Ser, Inside the subduction factory. https://doi.org/10.1029/138GM03.

Elliott, T., Plank, T., Zindler, A., White, W., Bourdon, B., 1997. Element transport from slab to volcanic front at the Mariana arc. J. Geophys. Res. 102, 14,991–15,019. https://doi.org/10.1029/97JB00788.

Eyuboglu, Y., Chung, S.-L., Santosh, M., Dudas, F., Akaryalı, E., 2011. Transition from shoshonitic to adakitic magmatism in the eastern Pontides, NE Turkey: Implications

for slab window melting. Gondwana Res. 19, 413–429. https://doi.org/10.1016/j.gr.2010.07.006.
Foley, S., 1992. Vein-plus-wall-rock melting mechanisms in the lithosphere and the origin of potassic alkaline magmas. Lithos 28, 435–453. https://doi.org/10.1016/0024-4937(92)90018-T.
Foley, S.F., Venturelli, G., Green, D.H., Toscani, L., 1987. The ultrapotassic rocks: Characteristics, classification, and constraints for petrogenetic models. Earth-Science Rev. 24, 81–134. https://doi.org/10.1016/0012-8252(87)90001-8.
Francalanci, L., Innocenti, F., Manetti, P., Savaşçin, M.Y., 2000. Neogene alkaline volcanism of the Afyon-Isparta area, Turkey: petrogenesis and geodynamic implications. Mineral. Petrol. 70, 285–312. https://doi.org/10.1007/s007100070007.
Freda, C., Gaeta, M., Palladino, D.M., Trigila, R., 1997. The Villa Senni Eruption (Alban Hills, Central Italy): the role of H2O and CO2 on the magma chamber evolution and on the eruptive scenario. J. Volcanol. Geotherm. Res. 78, 103–120. https://doi.org/10.1016/S0377-0273(97)00007-3.
Frezzotti, M.L., Peccerillo, A., Panza, G., 2009. Carbonate metasomatism and CO2 lithosphere–asthenosphere degassing beneath the Western Mediterranean: an integrated model arising from petrological and geophysical data. Chem. Geol. 262, 108–120. https://doi.org/10.1016/j.chemgeo.2009.02.015.
Grosjean, M., Moritz, R., Rezeau, H., Hovakimyan, S., Ulianov, A., Chiaradia, M., Melkonyan, R., 2022. Arabia-Eurasia convergence and collision control on Cenozoic juvenile K-rich magmatism in the South Armenian block. Lesser Caucasus. Earth-Sci. Rev. 226, 103949 https://doi.org/10.1016/j.earscirev.2022.103949.
Guarino, G., Solone, R., Casalini, M., Franciosi, L., Dallai, L., Morra, V., Conticelli, S., Melluso, L., 2022. The geochemistry of leucite-bearing lavas from early stages of the Somma-Vesuvius volcanic complex: Feeder systems and mantle enrichment processes in the Neapolitan district of the Roman Magmatic Province. Chem. Erde-Geochem. 126076 https://doi.org/10.1016/j.chemer.2023.126076.
Gülmez, F., Genç, Ş.C., Prelević, D., Tüysüz, O., Karacik, Z., Roden, M., Billor, Z., 2016. Ultrapotassic Volcanism from the waning stage of the Neotethyan Subduction: a Key Study from the Izmir–Ankara–Erzincan Suture Belt, Central Northern Turkey. J. Petrol. 57, 561–593. https://doi.org/10.1093/petrology/egw02.
Gülmez, F., Prelević, D., Förster, M.W., Buhre, S., Günther, J., 2023. Experimental production of K-rich metasomes through sediment recycling at the slab-mantle interface in the fore-arc. Sci. Rep. 13, 19608. https://doi.org/10.1038/s41598-023-46367-7.
Hart, S.R., 1984. A large-scale isotope anomaly in the Southern Hemisphere mantle. Nature 309, 753–757. https://doi.org/10.1038/309753a0.
Hastie, A., Kerr, A., Pearce, J., Mitchell, S., 2007. Classification of Altered Volcanic Island Arc Rocks using Immobile Trace elements: Development of the Th Co Discrimination Diagram. J. Petrol. 48, 2341–2357. https://doi.org/10.1093/petrology/egm062.
Innocenti, F., Agostini, S., Di Vincenzo, G., Doglioni, C., Manetti, P., Savaşçin, M., Tonarini, S., 2005. Neogene and Quaternary volcanism in Western Anatolia: Magma sources and geodynamic evolution. Mar. Geol. 221, 397–421. https://doi.org/10.1016/j.margeo.2005.03.016.
La Tourette, T.Z., Hervig, R.L., Holloway, J.R., 1995. Trace element partitioning between amphibole, phlogopite and basanite melt. Earth Planet. Sci. Lett. 135, 13–30. https://doi.org/10.1016/0012-821X(95)00146-4.
Le Maitre, R.W.L., Streckeisen, A., Zanettin, B., Bas, M.J.L., Bonin, B., Bateman, P., 2002. Igneous Rocks: A Classification and Glossary of terms. In: Recommendations of the International Union of Geological Sciences Subcommission on the Systematics of Igneous Rocks. Cambridge University Press.
Li, H., Hermann, J., Zhang, L., 2022. Melting of subducted slab dictates trace element recycling in global arcs. Sci. Adv. 8, eabh2166. https://doi.org/10.1126/sciadv.abh2166.
Lloyd, F.E., Arima, M., Edgar, A.D., 1985. Partial melting of a phlogopite-clinopyroxenite nodule from south-West Uganda: an experimental study bearing on the origin of highly potassic continental rift volcanics. Contrib. Mineral. Petrol. 91, 321–329. https://doi.org/10.1007/BF00374688.
Luhr, J.F., Kyser, T.K., 1989. Primary igneous analcime: the Colima minettes. Am. Mineral. 74, 216–223.
Lustrino, M., Wilson, M., 2007. The circum-Mediterranean anorogenic Cenozoic igneous province. Earth-Sci. Rev. 81, 1–65. https://doi.org/10.1016/j.earscirev.2006.09.002.
Lustrino, M., Fedele, L., Agostini, S., Prelević, D., Salari, G., 2019. Leucitites within and around the Mediterranean area. Lithos 324-325, 216–233. https://doi.org/10.1016/j.lithos.2018.11.007.
McQuarrie, N., van Hinsbergen, D.J., 2013. Retrodeforming the Arabia-Eurasia collision zone: Age of collision versus magnitude of continental subduction. Geology 41, 315–318. https://doi.org/10.1130/G33591.1.
Nagarajan, R., Madhavaraju, J., Armstrong-Altrin, J.S., Nagendra, R., 2011. Geochemistry of Neoproterozoic limestones of the Shahabad Formation, Bhima Basin, Karnataka, southern India. Geosci. J. 15, 9–25. https://doi.org/10.1007/s12303-011-0005-0.
Pearce, J., 1982. Trace element characteristics of Lavas from destructive plate boundaries. In: Orogenic Andesites, pp. 525–548.
Peccerillo, A., Taylor, S.R., 1976. Geochemistry of Eocene calc-alkaline volcanic rocks from the Kastamonu area, Northern Turkey. Contrib. Mineral. Petrol. 58, 63–81. https://doi.org/10.1007/BF00384745.
Prelević, D., Foley, S., Cvetković, V., Romer, R., 2004. The analcime problem and its impact on the geochemistry of ultrapotassic rocks from Serbia. Mineral. Mag. - Min. MAG 68, 633–648. https://doi.org/10.1180/0026461046840209.
Prelević, D., Foley, S., Romer, R., Cvetkovic, V., Downes, H., 2005. Tertiary Ultrapotassic Volcanism in Serbia: Constraints on Petrogenesis and Mantle Source Characteristics. J. Petrol. 46, 1443–1487. https://doi.org/10.1093/petrology/egi022.
Prelević, D., Foley, S.F., Romer, R., Conticelli, S., 2008. Mediterranean Tertiary lamproites derived from multiple source components in postcollisional geodynamics. Geochim. Cosmochim. Acta 72, 2125–2156. https://doi.org/10.1016/j.gca.2008.01.029.
Plank, T., Langmuir, C.H., 1998. The chemical composition of subducting sediment and its consequences for the crust and mantle. Chem. Geol. 145, 325–394. https://doi.org/10.1016/S0009-2541(97)00150-2.
Prelević, D., Akal, C., Foley, S.F., Stracke, A., Van Den Bogaard, P., 2012. Ultrapotassic Mafic Rocks as Geochemical Proxies for Post-collisional Dynamics of Orogenic Lithospheric Mantle: the Case of Southwestern Anatolia, Turkey. J. Petrol. 53, 1019–1055. https://doi.org/10.1093/petrology/egs008.
Prelević, D., Akal, C., Romer, R.L., Mertz-Kraus, R., Helvacı, C., 2015. Magmatic Response to Slab Tearing: Constraints from the Afyon Alkaline Volcanic complex, Western Turkey. J. Petrol. 56, 527–562. https://doi.org/10.1093/petrology/egv008.
Rabiee, A., Rossetti, F., Tecce, F., Asahara, Y., Azizi, H., Glodny, J., Lucci, F., Nozaem, R., Opitz, J., Selby, D., 2019. Multiphase magma intrusion, ore-enhancement and hydrothermal carbonatisation in the Siah-Kamar porphyry Mo deposit, Urumieh-Dokhtar magmatic zone, NW Iran. Ore Geol. Rev. 110, 102930 https://doi.org/10.1016/j.oregeorev.2019.05.016.
Ren, H., Casalini, M., Conticelli, S., Chen, C., Foley, S.F., Feng, L., Liu, Y., 2023. Calcium isotope compositions of subduction related leucite bearing rocks: implications for the calcium isotope heterogeneity of the mantle and carbonate recycling in convergent margins. Geochim. Cosmochim. Acta 364, 100–113. https://doi.org/10.1016/j.gca.2023.11.022.
Rustioni, G., Audetat, A., Keppler, H., 2021. The composition of subduction zone fluids and the origin of the trace element enrichment in arc magmas. Contrib. Mineral. Petrol. 176, 51. https://doi.org/10.1007/s00410-021-01810-8.
Saccani, E., 2015. A new method of discriminating different types of post-Archean ophiolitic basalts and their tectonic significance using Th-Nb and Ce-Dy-Yb systematics. Geosci. Front. 6, 481–501. https://doi.org/10.1016/j.gsf.2014.03.006.
Saccani, E., Allahyari, K., Beccaluva, L., Bianchini, G., 2013. Geochemistry and petrology of the Kermanshah ophiolites (Iran): Implication for the interaction between passive rifting, oceanic accretion, and OIB-type components in the Southern Neo-Tethys Ocean. Gondwana Res. 24, 392–411. https://doi.org/10.1016/j.gr.2012.10.009.
Sengor, A.M.C., Yilmaz, Y., 1981. Tethyan evolution of Turkey: a plate tectonic approach. Tectonophysics 75, 181–190. https://doi.org/10.1016/0040-1951(81)90275-4.
Shafaii Moghadam, H., Zaki Khedr, M., Chiaradia, M., Stern, R.J., Bakhshizad, F., Arai, S., Ottley, C.J., Tamura, A., 2014. Supra-subduction zone magmatism of the Neyriz ophiolite, Iran: constraints from geochemistry and Sr-Nd-Pb isotopes. Int. Geol. Rev. 56, 1395–1412. https://doi.org/10.1080/00206814.2014.942391.
Shafaii Moghadam, H., Griffin, W.L., Kirchenbaur, M., Garbe-Schönberg, D., Khedr, M.Z., Kimura, J.I., Stern, R.J., Ghorbani, G., Murphy, R., O'Reilly, S.Y., Arai, S., Maghdour-Mashhour, R., 2018. Roll-back, extension and mantle upwelling triggered eocene potassic magmatism in NW Iran. J. Petrol. 59, 1417–1465. https://doi.org/10.1093/petrology/egy067.
Skora, S., Blundy, J.D., Brooker, R.A., Green, E.C.R., de Hoog, J.C.M., Connolly, J.A.D., 2015. Hydrous phase Relations and Trace Element Partitioning Behaviour in Calcareous Sediments at Subduction-Zone Conditions. J. Petrol. 56, 953–980. https://doi.org/10.1093/petrology/egv024.
Soltanmohammadi, A., Grégoire, M., Rabinowicz, M., Gerbault, M., Ceuleneer, G., Rahgoshay, M., Bystricky, M., Benoit, M., 2018. Transport of volatile-rich melt from the mantle transition zone via compaction pockets: Implications for mantle metasomatism and the origin of Alkaline Lavas in the Turkish-Iranian plateau. J. Petrol. 59, 2273–2310. https://doi.org/10.1093/petrology/egy097.
Soltanmohammadi, A., Grégoire, M., Ceuleneer, G., Benoit, M., Bédard, L., Gouy, S., Rabinowicz, M., 2021. Origin of Antecrysts in Igneous Rocks from the Salavat Range (NW Iran): an Explanation for the Geochemical Signature of Potassic Alkaline Rocks. J. Petrol. 62, egab031. https://doi.org/10.1093/petrology/egab031.
Stampfli, G.M., 2000. Tethyan oceans. Geol. Soc. London Spec. Publ. 173, 1 LP–23. https://doi.org/10.1144/GSL.SP.2000.173.01.01.
Sun, S.S., McDonough, W.F., 1989. Chemical and isotopic systematics of oceanic basalts: implications for mantle composition and processes. Geol. Soc. London Spec. Publ. 42, 313–347.
Thomsen, T.B., Schmidt, M.W., 2008. Melting of carbonated pelites at 2.5–5.0 GPa, silicate–carbonatite liquid immiscibility, and potassium–carbon metasomatism of the mantle. Earth Planet. Sci. Lett. 267, 17–31. https://doi.org/10.1016/j.epsl.2007.11.027.
Todt, W., Cliff, R.A., Hanser, A., Hofmann, A.W., 1996. Evaluation of a 202Pb–205Pb Double Spike for High - Precision Lead Isotope Analysis. In: Earth Processes: Reading the Isotopic Code, Geophysical Monograph Series, pp. 429–437. https://doi.org/10.1029/GM095p0429.
Tommasini, S., Avanzinelli, R., Conticelli, S., 2011. The Th/La and Sm/La conundrum of the Tethyan realm lamproites. Earth Planet. Sci. Lett. 301, 469–478. https://doi.org/10.1016/j.epsl.2010.11.023.
Verdel, C., Wernicke, B.P., Hassanzadeh, J., Guest, B., 2011. A Paleogene extensional arc flare-up in Iran. Tectonics 30, TC3008. https://doi.org/10.1029/2010TC002809.